



HAL
open science

Numerical simulations of thermal convection on a hemisphere

C.-H Bruneau, Patrick Fischer, Y.-L. Xiong, H. Kellay

► **To cite this version:**

C.-H Bruneau, Patrick Fischer, Y.-L. Xiong, H. Kellay. Numerical simulations of thermal convection on a hemisphere. *Physical Review Fluids*, 2018, 3 (4), pp.043502. 10.1103/PhysRevFluids.3.043502 . hal-01803691

HAL Id: hal-01803691

<https://hal.science/hal-01803691>

Submitted on 30 May 2018

HAL is a multi-disciplinary open access archive for the deposit and dissemination of scientific research documents, whether they are published or not. The documents may come from teaching and research institutions in France or abroad, or from public or private research centers.

L'archive ouverte pluridisciplinaire **HAL**, est destinée au dépôt et à la diffusion de documents scientifiques de niveau recherche, publiés ou non, émanant des établissements d'enseignement et de recherche français ou étrangers, des laboratoires publics ou privés.

Numerical simulations of thermal convection on a hemisphere

C.-H. Bruneau and P. Fischer*

Univ. Bordeaux, IMB, CNRS UMR 5251, F-33400 Talence, France

Y.-L. Xiong

Huazhong Univ. Science and Technology, Sch. Civil Engineering and Mechanics, China

H. Kellay

Univ. Bordeaux, LOMA, CNRS UMR 5798, F-33400 Talence, France

(Cyclobulle Collaboration)



(Received 21 December 2017; published 16 April 2018)

In this paper we present numerical simulations of two-dimensional turbulent convection on a hemisphere. Recent experiments on a half soap bubble located on a heated plate have shown that such a configuration is ideal for studying thermal convection on a curved surface. Thermal convection and fluid flows on curved surfaces are relevant to a variety of situations, notably for simulating atmospheric and geophysical flows. As in experiments, our simulations show that the gradient of temperature between the base and the top of the hemisphere generates thermal plumes at the base that move up from near the equator to the pole. The movement of these plumes gives rise to a two-dimensional turbulent thermal convective flow. Our simulations turn out to be in qualitative and quantitative agreement with experiments and show strong similarities with Rayleigh-Bénard convection in classical cells where a fluid is heated from below and cooled from above. To compare to results obtained in classical Rayleigh-Bénard convection in standard three-dimensional cells (rectangular or cylindrical), a Nusselt number adapted to our geometry and a Reynolds number are calculated as a function of the Rayleigh number. We find that the Nusselt and Reynolds numbers verify scaling laws consistent with turbulent Rayleigh-Bénard convection: $Nu \propto Ra^{0.31}$ and $Re \propto Ra^{1/2}$. Further, a Bolgiano regime is found with the Bolgiano scale scaling as $Ra^{-1/4}$. All these elements show that despite the significant differences in geometry between our simulations and classical 3D cells, the scaling laws of thermal convection are robust.

DOI: [10.1103/PhysRevFluids.3.043502](https://doi.org/10.1103/PhysRevFluids.3.043502)

I. INTRODUCTION

The two-dimensional Navier-Stokes equations are often used as a model for describing turbulence in the atmosphere [1–3]. Indeed, atmospheric phenomena are confined in a layer of fluid whose dimensions are only a few kilometers in the vertical direction and thousands of kilometers in the horizontal directions. This implies that most of the kinetic energy of large-scale structures is actually embedded in the horizontal velocities. Even if this model cannot completely describe the complexity of the atmosphere, two-dimensional simulations can still be used to mimic large-scale structures in the atmosphere. Past two-dimensional turbulence simulations are often restricted to doubly periodic planar domains. Few studies deal with flow simulations on curved spaces as in Refs. [4,5], where space

*patrick.fischer@u-bordeaux.fr

curvature fluctuations are taken into consideration as metric perturbations. Other studies consider shallow-water turbulence on a sphere as in Ref. [6], but none of them consider thermal convection-induced turbulence (as in Rayleigh-Bénard convection [7,8]) on a curved space. Rayleigh-Bénard convection experiments are usually realized in parallelepipedic or cylindrical domains.

Quite recently, Refs. [9,10] designed a new physical experiment: a thermal convection cell composed by a half soap bubble heated at the equator. This device allowed them to study thermal convection and the movement of large-scale structures on the surface of the bubble. Similarities with atmospheric flows were suggested by such a study [9,11]. They showed in particular that the vortices on the bubble surface and tropical cyclones in the atmosphere have the same dynamics: in terms of trajectory [9,10] but also in terms of intensity [11]. This system as it is heated on one side (the equator) showed intense thermal convection leading to turbulent velocity and temperature fields whose statistical properties can be described by theories of turbulent thermal convection elaborated by Refs. [9,10]. In short, a hemispherical bubble heated at the equator is an excellent system, which allows to study thermal convection without the presence of lateral walls and to explore a variety of physical phenomena of relevance to atmospheric and geophysical flows.

Nevertheless, the exact details of the properties of convection on the global scale of the bubble such as heat transfers, energy spectra and fluxes of different quantities have not been obtained experimentally due to experimental difficulties. The purpose of this paper is to present new numerical simulations (different from Refs. [11,12]) of thermal convection in such an unusual system: a hemispherical cap heated at the equator. We carry out a complete study for a wide range of Rayleigh numbers and examine the details of heat transfers through the variation of the Nusselt number versus the Rayleigh number as well as through direct measurements of the fluxes of energy, enstrophy, and entropy along with their associated spectra. We compare our results to known behavior in classical Rayleigh-Bénard convection in three-dimensional containers. We are, in particular, able to detect a Bolgiano regime in an area far from the boundary layers (which are located above the equator) that does not include the pole. This regime is usually observed in Rayleigh-Bénard turbulence but also in Rayleigh-Taylor turbulence [13]. Numerical experiments in a geometrically confined turbulent Rayleigh-Taylor system, where one dimension is much smaller than the other two, have been performed by Boffetta *et al.* [14]. They showed that when the size of the mixing layer becomes larger than the smallest dimension, the system becomes two-dimensional and the Bolgiano scale is then associated to the smallest dimension of the system. In our numerical experiments, the geometrical setup is completely different, and the zero-crossing points of the fluxes (energy, enstrophy, and entropy) are shown to be good indicators of the behavior of the Bolgiano scale with respect to the Rayleigh number.

Using a stereographic transform, we project the Navier-Stokes equations onto a plane and use regular Cartesian grid-based methods to numerically solve the equations. The model is described in Sec. II, the numerical methods are described in Sec. III, and the results are analyzed and discussed in Sec. IV.

II. THE MODEL AND THE EQUATIONS IN THE STEREOGRAPHIC COORDINATES

A. The model

Rayleigh-Bénard convection [7,8] is an idealized version of thermal convection found in industrial and natural settings. It is useful for understanding convective flows in the atmosphere, in astrophysics, in geophysical flows, etc. In this classical model, a horizontal layer of incompressible fluid confined between two flat plates is heated from below and cooled at the top. Depending on the boundary conditions (free-slip or no-slip conditions) and depending on various physical parameters of the fluid (Rayleigh and Prandtl numbers) different behaviors have been observed: oscillatory, chaotic, or turbulent convection [15].

But here, as mentioned above, the present experiment does not correspond to any classical two-dimensional turbulence set up and the only walls present are those at the equator. So our first task is to

understand the underlying behavior of the flows and the fluxes (of heat and momentum) present and to write down the mathematical equations in the correct coordinate system allowing us to describe flows in hemispherical geometry. As the relevant fluid flow and heat flux equations do not depend on the coordinate system, the fluid behavior can be described using the equations for the two-dimensional thermal convection under the Boussinesq approximation [16] as

$$\begin{aligned}\frac{D\mathbf{U}}{Dt} &= -\frac{1}{\rho}\nabla p + \nu\nabla^2\mathbf{U} - \beta T\mathbf{g} - \tilde{F}\mathbf{U}, \\ \nabla \cdot \mathbf{U} &= 0, \\ \frac{DT}{Dt} &= \alpha\nabla^2 T - \tilde{S}T,\end{aligned}\tag{1}$$

where $\frac{D}{Dt} \equiv \frac{\partial}{\partial t} + (\mathbf{U} \cdot \nabla)$, is the total time derivative, \mathbf{U} denotes the velocity, p the pressure, ρ the mass density, ν the kinematic viscosity, β the coefficient of thermal expansion, \mathbf{g} the gravity field, T the temperature of the fluid, α the coefficient of thermal diffusion, \tilde{F} is the friction factor, and \tilde{S} is the thermal dissipation coefficient. The terms $\tilde{F}\mathbf{U}$ and $\tilde{S}T$ have been added to compensate, respectively, the injection of kinetic and thermal energies. Dimensionless equivalent of \tilde{F} and \tilde{S} have been empirically evaluated to reach a stationary state, their values are discussed in Sec. IV A.

B. The Navier-Stokes equations in stereographic coordinates

Using the calculations detailed in the Appendices, the Navier-Stokes Eqs. (1) for a hemisphere of radius $r = 1$ can thus be written using stereographic coordinates:

$$\begin{aligned}\frac{\partial u}{\partial t} + u\frac{\partial u}{\partial x} + v\frac{\partial u}{\partial y} + \frac{2}{1+x^2+y^2}(-xu^2 - 2yuv + xv^2) \\ = v\left[\frac{(1+x^2+y^2)^2}{4}\left(\frac{\partial^2 u}{\partial x^2} + \frac{\partial^2 u}{\partial y^2}\right) - u - (1+x^2+y^2)\left(x\frac{\partial u}{\partial x} + y\frac{\partial u}{\partial y} + y\frac{\partial v}{\partial x} - x\frac{\partial v}{\partial y}\right)\right] \\ - \frac{1}{\rho}\left(\frac{1+x^2+y^2}{2}\right)^2\frac{\partial p}{\partial x} - x\beta gT - \tilde{F}u, \\ \frac{\partial v}{\partial t} + u\frac{\partial v}{\partial x} + v\frac{\partial v}{\partial y} + \frac{2}{1+x^2+y^2}(yu^2 - 2xuv - yv^2) \\ = v\left[\frac{(1+x^2+y^2)^2}{4}\left(\frac{\partial^2 v}{\partial x^2} + \frac{\partial^2 v}{\partial y^2}\right) - v - (1+x^2+y^2)\left(x\frac{\partial u}{\partial y} - y\frac{\partial u}{\partial x} + x\frac{\partial v}{\partial x} + y\frac{\partial v}{\partial y}\right)\right] \\ - \frac{1}{\rho}\left(\frac{1+x^2+y^2}{2}\right)^2\frac{\partial p}{\partial y} - y\beta gT - \tilde{F}v,\end{aligned}\tag{2}$$

$$\frac{\partial u}{\partial x} + \frac{\partial v}{\partial y} = \frac{4(xu + yv)}{1+x^2+y^2},\tag{3}$$

$$\frac{\partial T}{\partial t} + u\frac{\partial T}{\partial x} + v\frac{\partial T}{\partial y} = \alpha\frac{(1+x^2+y^2)^2}{4}\left(\frac{\partial^2 T}{\partial x^2} + \frac{\partial^2 T}{\partial y^2}\right) - \tilde{S}T.\tag{4}$$

The stereographic projection transforms the Navier-Stokes equations into a complicated expression (compared to the usual cartesian coordinates formulation) adding some extra terms. However, one can still recognize the various terms and we can now apply usual numerical methods to solve the equations on cartesian grids.

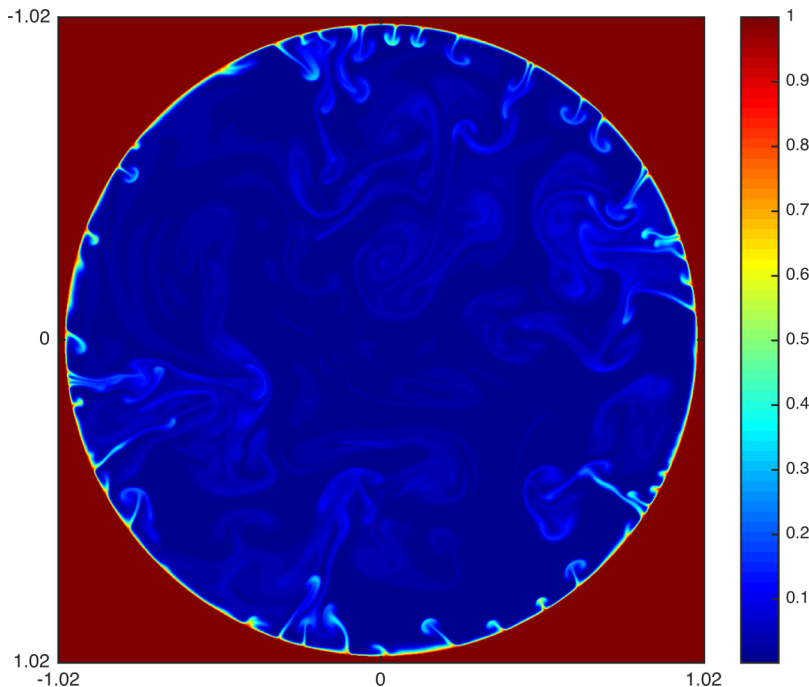


FIG. 1. Temperature field in the equatorial plane at $Ra = 3 \times 10^9$ and $Pr = 7$. The Cartesian grid is defined on a square larger than the bubble, and the corners are taken into consideration thanks to a penalization method.

III. NUMERICAL APPROXIMATIONS OF THE NAVIER-STOKES EQUATIONS IN STEREOGRAPHIC COORDINATES

A L^2 -penalization method is used to define the circular domain in the equatorial plane and to set a no-slip boundary condition on the equator, as well as a Dirichlet boundary condition for T . The boundaries are actually considered like a porous medium of very low permeability and taken into account by the volume penalization procedure which consists in adding two penalization terms, $\frac{\mathbf{U}-\mathbf{U}_b}{C}$, in the momentum equation and $\frac{T-T_b}{C}$, in the temperature equation, which are now set on the whole squared domain [17]. In our numerical simulations, C is set equal to 10^{16} in the bubble and equal to 10^{-10} outside. The boundary conditions are then imposed by taking $\mathbf{U}_b = 0$ and $T_b = 1$. When $C = 10^{16}$ in the bubble, these extra terms vanish and we solve the regular Eqs. (1), and when $C = 10^{-10}$ outside the bubble, all the other terms are numerically very small compared to the extra terms and we thus have $\mathbf{U} = 0$ and $T = 1$. A sample of the temperature field is given in Fig. 1.

Finite differences schemes are used for solving the equations described in the previous part. The spatial domain is discretized with a staggered uniform Cartesian grid with a mesh size $l = \delta x = \delta y$, where δx and δy are the discretization steps in each direction on the projection plane. The time interval is partitioned with uniform time steps δt . A second-order Gear scheme is used to solve the unsteady term in the governing equations. The linear terms are solved using an implicit scheme, whereas the convection terms are solved using an explicit one. If one denotes by \mathbf{u}^n the approximation of \mathbf{u} at time $t_n = n\delta t$, then the approximation of the total time derivative of a general variable ϕ using the second-order Gear scheme can be written as

$$\frac{D\phi}{Dt} \approx \frac{3\phi^n}{2\delta t} - \frac{4\phi^{n-1} - \phi^{n-2}}{2\delta t} + 2(\mathbf{u}^{n-1} \cdot \nabla)\phi^{n-1} - (\mathbf{u}^{n-2} \cdot \nabla)\phi^{n-2}. \quad (5)$$

The discrete values of the pressure p and the temperature T are located at the center of each cell and the discrete values of the velocity field are located at the middle of the cell sides as shown in

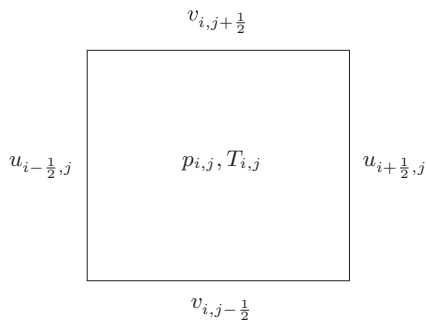


FIG. 2. A staggered cell. The pressure and the temperature are computed at the center of the cell. The velocity components are computed in the middle of the cell borders.

Fig. 2. The convection terms are approximated by a third-order Murman-like scheme. A detailed study of this kind of scheme can be found in Ref. [18]. Since the temperature equation can be solved separately, a time splitting has been used to first solve the temperature equation and then the coupled pressure and velocity equations. Both of them are solved in a parallel way in a cluster by message passing interface (MPI).

The discretization of the temperature equation leads to a linear system of equations $AT = E$, where A is a pentadiagonal matrix, T is the temperature vector, and E is the explicit part of the discretized temperature equation. However, the matrix A is not a self-adjoint matrix anymore in our present curved surface problem and we have to solve this linear problem using a biconjugated gradient method.

The discretization of the coupled velocity-pressure system of equations leads to solving a discrete linear system $L_l V_l^n = B_l^{n-1}$, where L_l represents the discrete operator, B_l^{n-1} is the discrete equivalent of the right-hand side of Eq. (5), and $V_l^n = (\mathbf{u}_l^n, p_l^{n+1/2})$ is the approximate solution we are looking for.

We have performed a grid convergence analysis to verify that the grid is dense enough to describe a turbulent flow. We have computed the global temperature on the bubble for different sizes of the grid and for a given Rayleigh number.

The results obtained with the 1024×1024 and 2048×2048 are almost exactly the same, whereas the results obtained with coarser grids (256×256 and 512×512) are slightly different. As it will be shown below, a fine grid (2048×2048) is better to describe the boundary layer at the equator, but does not improve the results in the bulk of the bubble. The grid 1024×1024 has thus been chosen in the following for analyzing the results, but a few results obtained with the 2048×2048 grid are given in the part discussing the boundary layer thickness. To focus on the physics of the problem and not on the numerical aspects, the results presented and analyzed in the present article have been obtained with a classical single-grid process and not with the more sophisticated multigrid approach described in Refs. [11,12].

IV. NUMERICAL RESULTS AND ANALYSIS

The results with Rayleigh numbers $Ra = \frac{g\beta L^3 \delta T}{\nu\alpha}$ [where δT denotes the difference of temperature between the pole and the equator, and L the characteristic length equal to the radius of the bubble ($L = r$)] from 10^6 to 10^{10} are analyzed in this part. The equations are made nondimensional by using L , δT and the characteristic velocity $U = \sqrt{\beta g \delta T L}$. Thus, the control parameters in our numerical simulations are the Rayleigh number Ra and the Prandtl number Pr . Besides, we get the dimensionless friction factor $F = \frac{\bar{r}L}{U}$ and the dimensionless thermal dissipation coefficient $S = \frac{\bar{r}L}{U}$. The goal of these dimensionless factors is to take into consideration the interaction between the

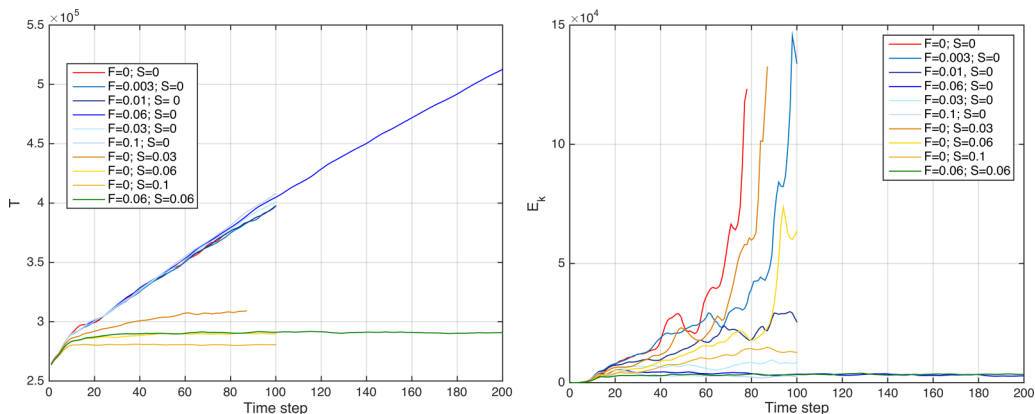


FIG. 3. Evolution of the thermal (left) and kinetic (right) total energies with time for various values of the stabilization parameters F and S at $Ra = 3 \times 10^8$ and $Pr = 7$. Computations with $\delta t = 5 \times 10^{-4}$ with outputs every 2000 time steps. Total time steps : $200 \times 2000 = 400\,000$.

bubble and the air. The empirical evaluation of their respective values is described in the following part.

A. Emergence of the stationary state

We present here the empirical analysis that leads to the stationary state for $Ra = 3 \times 10^8$. The time step has been chosen equal to 0.0005 with outputs every 2000 time steps. If the parameters F and S are kept equal to zero, one can observe an accumulation of kinetic and thermal energies leading to a numerical burst of the bubble. In usual Rayleigh-Bénard experiments the top plate is cooled allowing to keep a constant global averaged temperature. In the experiments on soap bubbles, the exchange of heat between the bubble and the surrounding air and the friction with the air stabilize experimental conditions. In our numerical simulations, we have to artificially remove a small part of thermal and kinetic energies to stabilize the computations. This stabilization process can be interpreted as a way to take into consideration the interaction between the bubble and the surrounding air. Different values for the parameters F and S have been tested to stabilize the computations. Results are reported in Fig. 3 for the total kinetic and thermal energies. As can be observed in Fig. 3, the bubble can be stabilized with $F = 0.06$ and $S = 0.06$. For these values, computations have been carried out for up to 400 000 time steps to verify that the simulations are really stabilized. Furthermore, these values have been verified as valid for different Rayleigh and Prandtl numbers. Removing uniformly about 6% of the temperature and of the velocity fields does not modify the convection versus conduction balance.

Let us now describe some qualitative features of the flows obtained. At the base of the bubble, thermal plumes are clearly visible Fig. 4. In the beginning of our simulation, the experiment is similar to a long two-dimensional toric Bénard cell: the cold fluid is heated from below, and the plumes are pushed upward. There is no interaction between the plumes and the center of the domain remains empty. These small structures emerging from the heated equator can be easily spotted on the vorticity field. Then the plumes continue to grow and start to interact with each other over time, and the small structures along the equator are now giving birth to vortices that move along the bubble surface as can be observed in Fig. 5.

B. The Rayleigh number dependence of the Nusselt and Reynolds numbers

Several studies describing Rayleigh-Bénard experiments have been carried out during the last few decades. Some of them describe physical experiments and others numerical simulations. The

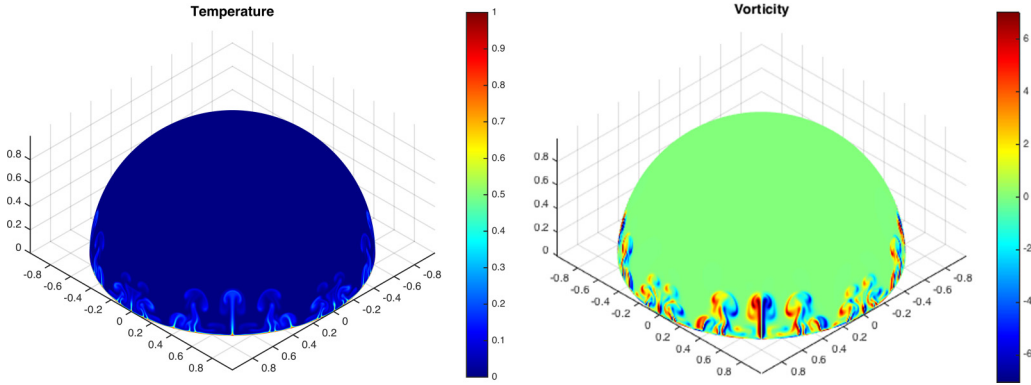


FIG. 4. Temperature (left) and vorticity (right) fields in the beginning of the simulation at $Ra = 3 \times 10^8$ and $Pr = 7$. Mushroom shape structures are created at the equator.

analysis of the Rayleigh dependence of the Nusselt number (which measures the heat transfer in the bubble) and the Reynolds number (which measures the strength of the turbulence) have been the focus of most studies. One of the most discussed problems being the existence of an ultimate regime for very high Rayleigh numbers experiments as predicted by Kraichnan [2]. The transition (in terms of the Rayleigh number) to this ultimate regime is not clearly established and is dependent on the geometry. Indeed, it has been shown that the presence of the ultimate regime is linked to the absence of the boundary layers by Boffetta *et al.* in Ref. [13]. As it will be shown in the sequel, the boundary layers (thermal and kinetic) close to the equator play an important role in our numerical experiments and no ultimate state has been observed. At least up-to the Rayleigh numbers achieved in our simulations. The reader might be interested by the work of Grossmann and Lohse, where a unifying theory that describes the heat transfer in a nonrotating Rayleigh-Bénard system is proposed [19–24].

Since our numerical simulations do not correspond to the classical Rayleigh-Bénard geometry, we cannot directly compare our scalings to the ones predicted by their theory. We can, however, consider three different areas in our bubble: around the pole, above the equator, and the area in between these two delimited areas. We present first the results obtained for the Nusselt and Reynolds numbers on

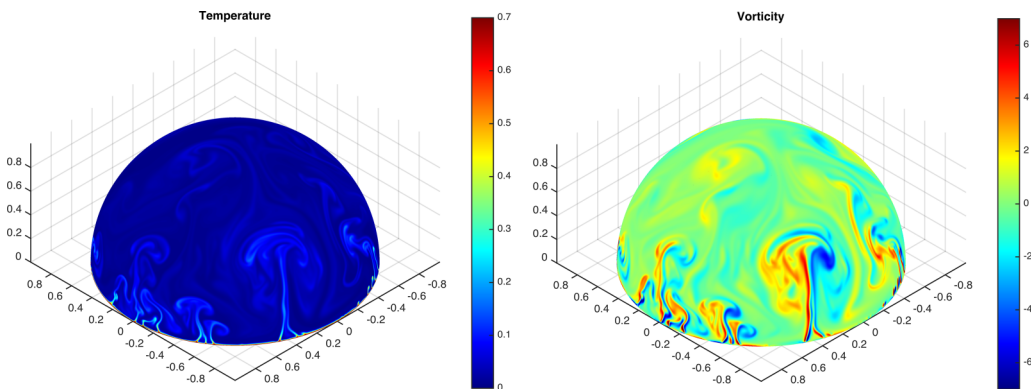


FIG. 5. Temperature (left) and vorticity (right) fields in the stationary state at $Ra = 3 \times 10^8$ and $Pr = 7$. Plumes move up on the bubble and the structures start to interact one with each other.

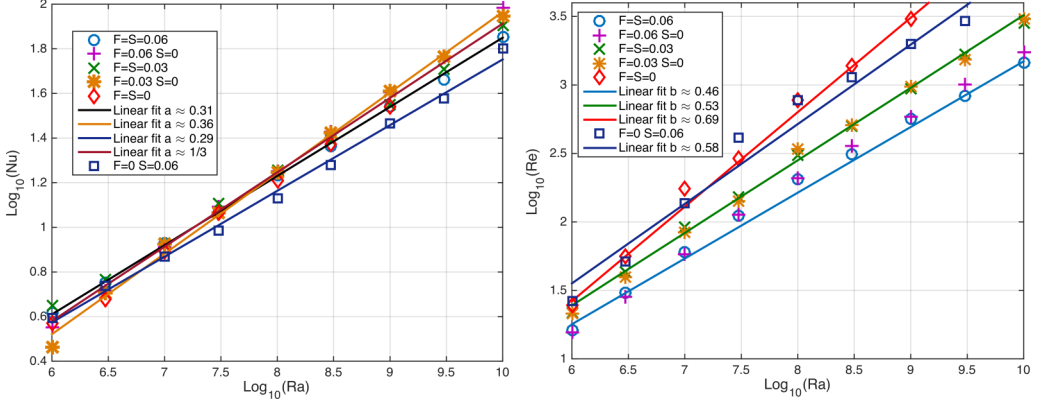


FIG. 6. Global Nusselt number (left) and Reynolds number (right) versus Rayleigh number at $\text{Pr} = 7$ for $F = S = 0$, $F = S = 0.03$, and $F = S = 0.06$.

the whole bubble. For a given latitude l , we can define the local Nusselt number $\text{Nu}(l)$ as

$$\text{Nu}(l) = \frac{\langle \mathbf{u}_{k_0} T \rangle_l - \alpha \partial_{k_0} \langle T \rangle_l}{\alpha \delta T L^{-1}}, \quad (6)$$

where \mathbf{u}_{k_0} denotes the vertical component of the velocity, T the temperature, $\langle \cdot \rangle_l$ the average in time and over a latitude l . The global Nusselt number Nu is then obtained by averaging the local Nusselt number over all the latitudes. The notion of “local” and “global” Nusselt numbers are not common in classical Rayleigh-Bénard experiments because a constant heat transfer is established in such experiments. Thus, a Nusselt number can be calculated by averaging over any horizontal plane. But local and global Nusselt numbers are used when the heat transfer depends on the height, as in an open channel or on our bubble experiment (see Eqs. (4) and (5) in Ref. [25], for instance). The global Nusselt number can then be studied as a function of the Rayleigh number. It can be seen as a global indicator of the convection versus conduction balance in the cell. Also, as stated above, the source terms (proportional to F and S) added to stabilize the computations are necessary to evaluate the correct heat transfer from the equator to the pole. Without this stabilization, we observe an accumulation of heat in the bubble that does not correspond to the physical experiment. The source terms are thus necessary to describe the correct heat transfer that takes place in the soap bubble and do not modify the convection versus conduction balance. In particular, we have verified for all Rayleigh numbers from $\text{Ra} = 10^6$ to $\text{Ra} = 10^{10}$ that the source terms do not significantly modify the Nusselt number. The influence of the source terms on the Nusselt and Reynolds numbers is detailed in the sequel.

Removing uniformly the same percentage of heat and kinetic energy does not modify the convection/conduction ratio, and thus does not modify the Nusselt number. This can be verified in Fig. 6, where the Nusselt numbers for $\text{Ra} = 10^6$ to $\text{Ra} = 10^9$ with $F = S = 0$ and $F = S = 0.03$ have been added to the plot. As can be observed, except for minor differences at low Rayleigh numbers, the Nusselt number verifies exactly the same scaling for $F = S = 0.06$ and $F = S = 0.03$ as for $F = S = 0$. So, if we consider only homogeneous source term parameters ($F = S$), we do not modify the Nusselt number. But if we consider nonhomogeneous parameters ($F \neq S$), then the Nusselt number scaling exponent ranges from 0.29 to 0.36 around a mean value of $1/3$. This can be observed in the left part of Fig. 7. So, we can conclude that the values necessary to reach a stationary state do not modify the heat transfers.

Since the Reynolds number (defined as $\text{Re} = \frac{\langle \mathbf{u} \rangle L}{\nu}$) is the ratio of inertial forces to viscous forces, it is slightly modified by the friction term, which removes part of the kinetic energy. As can be observed in the right part of the Fig. 6, the action of the friction term is to decrease the Reynolds number, and thus also modifies the scaling law if we consider a single linear fit for homogeneous

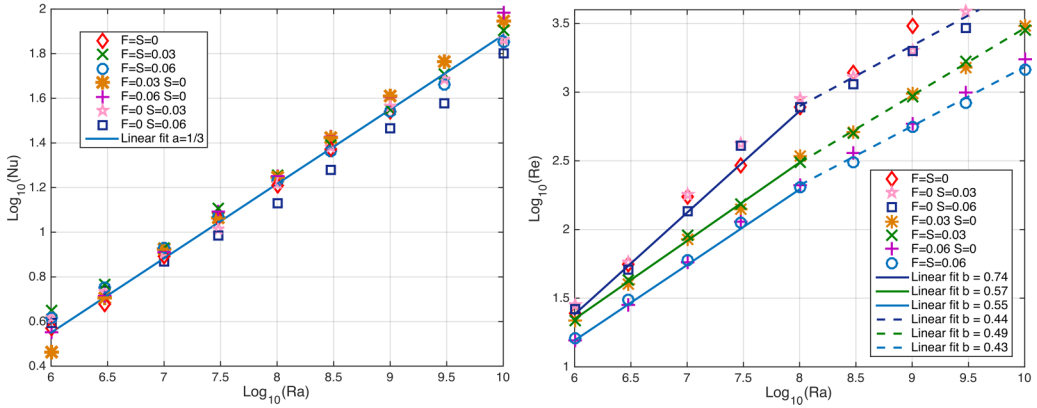


FIG. 7. Global Nusselt number (left) and Reynolds number (right) versus Rayleigh number at $Pr = 7$.

source parameters. But if we consider in-homogeneous source parameters ($F \neq S$) we can observe (right part of Fig. 7) that the friction parameter F is the main factor for the Reynolds number. We can observe three behaviors depending on the value of F : $F = 0$; $F = 0.03$; or $F = 0.06$. Furthermore, with double linear fits, the slopes for $F = 0.03$ and $F = 0.06$ are almost the same: around 0.56 for low Rayleigh numbers and around 0.44 for high Rayleigh numbers. We can also notice that the slope for high Rayleigh numbers for $F = 0$ is not too far either: around 0.49. However, the slope of low Rayleigh numbers for $F = 0$ is quite different: around 0.74.

We recall here that these source terms represent the interactions between the bubble and the surrounding air. Contrarily to the classical Rayleigh-Bénard convection, there is no cooled top plate in our experiment and these terms with $F = S = 0.06$ are necessary to obtain a stationary state.

For the stationary state simulations ($F = S = 0.06$), the global Nusselt number Nu versus the Rayleigh number Ra is given in Fig. 8. We can observe that the exponent in the $Nu \propto Ra^a$ correlation follows $a \approx 0.31$ over the full range of Rayleigh numbers, whereas we observe two scaling regimes in the $Re \propto Ra^b$ correlation, $b \approx 0.55$ for $10^6 \leq Ra \leq 10^8$ and $b \approx 0.43$ for $10^8 \leq Ra \leq 10^{10}$. This scaling for the global Nusselt number has been observed in many previous experiments [26–31] and numerical simulations [32] and is not too far from the classical theoretical prediction of $1/3$. So, it seems that the exponent of 0.31 is a characteristic of the heat transfer itself in thermal convection

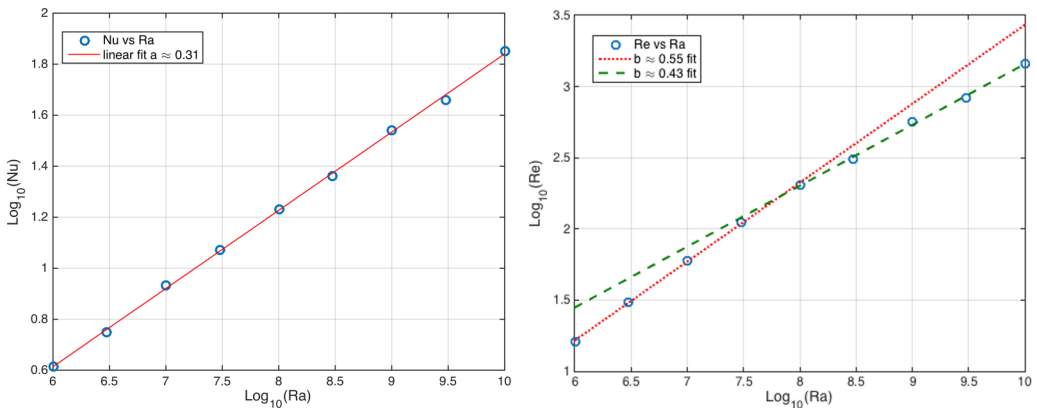
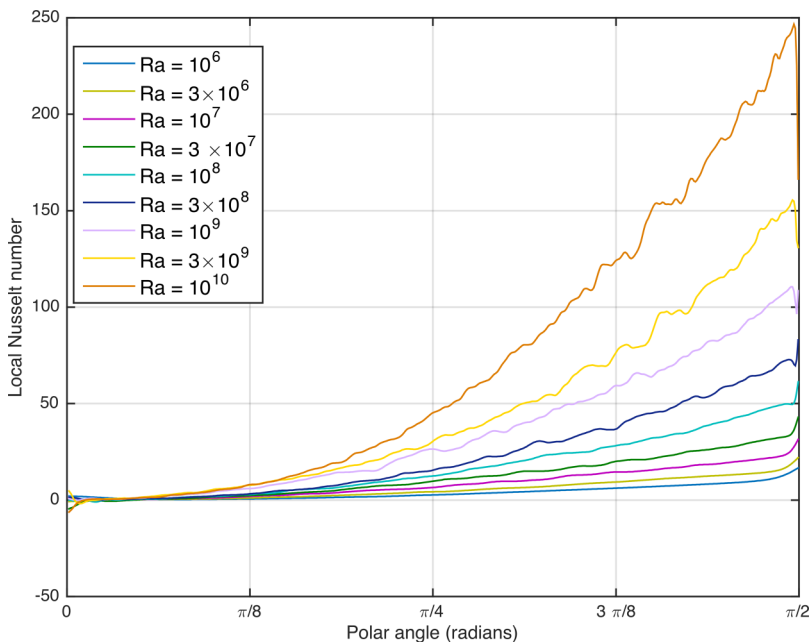


FIG. 8. Global Nusselt (left) and Reynolds (right) numbers versus Rayleigh number at $Pr = 7$. Scaling laws can be clearly observed.

FIG. 9. Local Nusselt numbers versus latitude (radians) at $Pr = 7$.

and is not dependent on geometry. Furthermore, the two scalings observed for the Reynolds number suggest that two different regimes exist in the range $10^6 \leq Ra \leq 10^{10}$, the transition being located around $Ra \approx 10^8$. It can be noticed that these scalings are not too far from the scalings of the regime I_l described by Grossmann and Lohse in Refs. [19–23].

Additional insight into heat conduction in this geometry considered here comes from examining the local Nusselt number variation. Contrary to the classical Rayleigh-Bénard setup, there is no symmetry between a top plate and a bottom plate in our simulations. The bubble is heated from below, but there is no continuous cooling at the top. Thus, the strongest heat flux is located near the equator (Fig. 9). The Nusselt and Reynolds numbers evaluated in an equatorial band (from 60° to 90°) are almost the same: power-law scaling with exponent 0.318 for the Nusselt number and the two regimes with exponents around 0.555 and 0.482 for the Reynolds number. Looking at Fig. 9, one reason that explains why the scalings $[Nu(Ra)]$ and $[Re(Ra)]$ are slightly different in the equatorial band comes from the following observation. If we study the average temperature versus latitude for different Rayleigh numbers, we observe that the boundary layer above the equator is decreasing as the Rayleigh number is increasing. This can be observed on the vorticity and temperature fields for $Ra = 10^6$ and $Ra = 10^{10}$ given in Figs. 10 and 11 and in Fig. 12. The temperature is quickly decreasing from 1 at the equator to almost 0 at the pole. For high Rayleigh number values, the boundary layer is very thin and the results are influenced by the size of the discretization step (1/512 in our numerical simulations: 1024×1024 for a bubble of radius 1). Many definitions for the boundary layer thickness can be found in the literature. We propose here a simple method for studying the boundary layer thickness, the 90% rule: for each averaged temperature curve we can localize the point where the temperature is around 0.1 (one-tenth of the thermal forcing) and we can measure the size ϵ of the boundary layer at this level. If we plot this length ϵ as a function of the Rayleigh number in a doubly logarithmic plot, then we obtain Fig. 14, where a scaling exponent of ≈ -0.3146 can be detected.

However, to verify that our method gives us the information we are looking for, we have also evaluated the boundary layer thickness using three classical methods [33–35]:

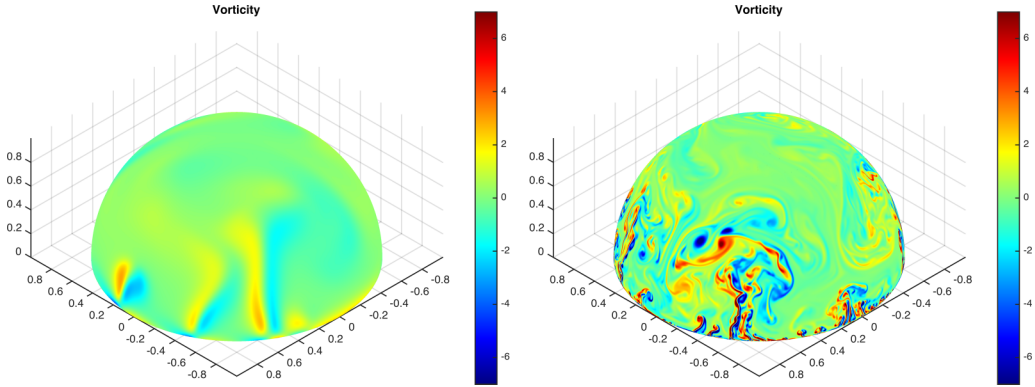


FIG. 10. Vorticity fields at $Pr = 7$ for $Ra = 10^6$ (left) and $Ra = 10^{10}$ (right). Many more structures can be observed in the more convective numerical experiment.

(1) Evaluation of the thickness based on the slope of the temperature profile at the wall: the distance at which the extrapolation of the linear portion of the mean profile equals the central mean temperature T_c (defined as the mean temperature in the bulk of the bubble).

(2) Peak of the root-mean square (RMS) of the temperature fluctuations.

(3) Since our mean-temperature profiles show a short linear part, we can fit the temperature profile in the equator area by a quadratic function $Q(l) = al^2 + bl + c$ (where l is the polar angle in radians and a , b , and c are fitting parameters), and then compute $\epsilon = \frac{2T_c + (a\pi + b)\pi - 1}{2(a\pi + b)}$ that corresponds to the intersection of the linear part of the quadratic fit with the central mean temperature T_c .

The RMS of the temperature fluctuations are given in Fig. 13 and the evolution of the boundary layer versus the Rayleigh number evaluated by the four methods previously described are given in Fig. 14. As can be observed in Fig. 14, the evaluation of the true value of the boundary layer thickness for large Rayleigh numbers is influenced by the discretization step size. So, we have performed the computations on a finer grid for $Ra = 3 \times 10^9$ and $Ra = 10^{10}$. If we zoom in on the RMS of the temperature fluctuations close to the equator for $Ra = 3 \times 10^9$ and $Ra = 10^{10}$, we can observe (Fig. 15) that the boundary layer thickness is in the limit of our discretization step size. This numerical limit for high Rayleigh numbers is also observed in experimental studies (see, for instance, Ref. [34]) when the distance between the sensor and the plate becomes comparable to the size of the sensor.

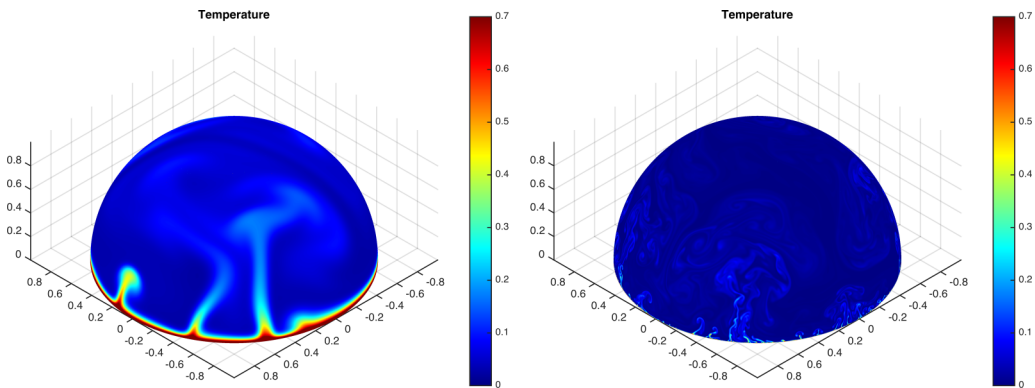


FIG. 11. Temperature fields at $Pr = 7$ for $Ra = 10^6$ (left) and $Ra = 10^{10}$ (right). Many more structures can be observed in the more convective numerical experiment.

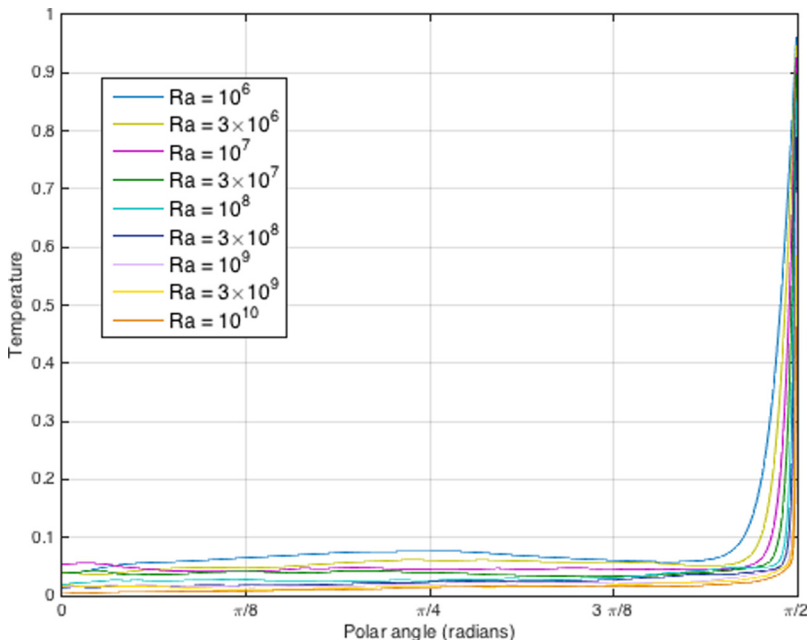


FIG. 12. Averaged temperature as a function of the latitude (rad.) for various Rayleigh number simulations at $Pr = 7$. Evolution of the boundary layer length can be clearly observed.

The three methods give the same values for the boundary layer thickness at low-medium Rayleigh numbers, but start to differ for high Rayleigh numbers (3×10^9 and 10^{10}). The slope calculated with the RMS method for eight Rayleigh number values (10^{10} being put apart) is about ≈ -0.3156 , similar to the value we have obtained with our method (which is not influenced by the discretization step size). Thus, this scaling law confirms the correlation between the Nusselt number and the boundary layer length. A large boundary layer length corresponds to heat transfer dominated by conduction normal to the boundary thus leading to a Nusselt number close to one. The Nusselt number increases at the same rate as the boundary layer length decreases with the Rayleigh number. So, our results confirm that the Nusselt number, which measures the balance between conductive versus convective heat transfer, is inversely proportional to the boundary layer length.

C. Spectra and fluxes

1. Spherical harmonics decomposition

Global properties, such as spectra or fluxes, for our numerical simulations can be obtained using mathematical tools specifically designed for spherical problems. We first recall the definitions of the spherical harmonics decomposition and then use them for computing these various physical indicators (spectra and fluxes) of interest.

Any function with spherical symmetry can be easily written as a linear combination of special functions $\{Y_k^m\}$,

$$f(\theta, \varphi) = \sum_{k=0}^{+\infty} \sum_{m=-k}^{+k} f_k^m Y_k^m(\theta, \varphi), \quad (7)$$

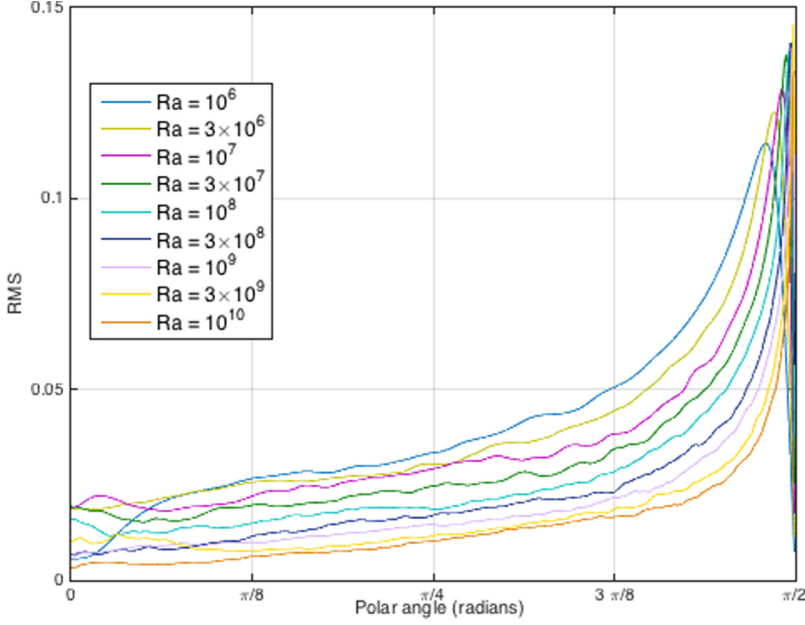


FIG. 13. RMS of the temperature fluctuations as a function of the polar angle for various Rayleigh numbers at $Pr = 7$. It is used as a proxy for the thermal boundary layer.

the so-called spherical harmonics defined by

$$Y_k^m(\theta, \varphi) = \sqrt{\frac{2k+1}{4\pi} \frac{(k-m)!}{(k+m)!}} P_k^m(\cos(\theta)) e^{im\varphi}. \quad (8)$$

Here, $P_k^m(\cdot)$ denotes the associated Legendre polynomials. The expansion coefficients f_k^m are then obtained by projection of f onto the spherical harmonics:

$$\begin{aligned} f_k^m &= \int_0^{2\pi} \int_0^{\pi/2} f(\theta, \varphi) \overline{Y_k^m(\theta, \varphi)} \sin(\theta) d\theta d\varphi \\ &= \sqrt{\frac{2k+1}{4\pi} \frac{(k-m)!}{(k+m)!}} \int_0^{2\pi} \int_0^{\pi/2} f(\theta, \varphi) P_k^m(\cos(\theta)) e^{-im\varphi} \sin(\theta) d\theta d\varphi. \end{aligned} \quad (9)$$

The integration over φ is actually a Fourier transform and is numerically computed with a traditional routine. The power spectrum can then be computed from the coefficients f_k^m :

$$\|f\|^2 = \sum_{k=0}^{+\infty} f_k^2 = \sum_{k=0}^{+\infty} \sum_{m=-k}^k |f_k^m|^2. \quad (10)$$

The coefficients f_k^m are thus equivalent to the Fourier coefficients and the coefficients f_k are equivalent to the Fourier wave numbers in a traditional Fourier power spectrum. We will call in the sequel *entropy* the thermal energy defined as

$$\|T\|^2 = \sum_{k=0}^{+\infty} T(k)^2 = \sum_{k=0}^{+\infty} \sum_{m=-k}^k |T_k^m|^2, \quad (11)$$

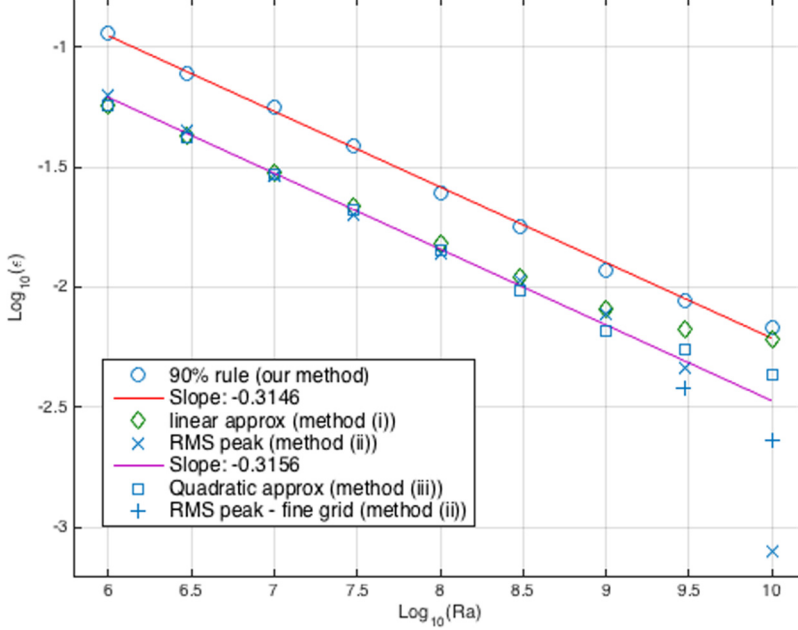


FIG. 14. Boundary layer size measured by various methods, as a function of the Rayleigh number at $\text{Pr} = 7$. All the methods lead to the same scaling of the boundary layer with respect to the Rayleigh number.

where

$$T_k^m = \int_0^{2\pi} \int_0^{\pi/2} T(\theta, \varphi) \overline{Y_k^m(\theta, \varphi)} \sin(\theta) d\theta d\varphi. \quad (12)$$

The spherical harmonics coefficients can also be used to compute energy, enstrophy, and entropy fluxes. We recall that the usual energy flux is computed from the nonlinear term in the Navier-Stokes equation written in Fourier space:

$$\Pi_E(k) = \int_k^{+\infty} S_E(k') dk', \quad (13)$$

where $S_E(k)$ is the nonlinear energy transfer function and is obtained by angular integration of $\widehat{v^*(\mathbf{k})} \cdot (\mathbf{v} \cdot \nabla) \widehat{v(\mathbf{k})}$. Here, the symbol $\widehat{\cdot}$ denotes the usual Fourier transform. The enstrophy and entropy fluxes are obtained in the same way:

$$\Pi_Z(k) = \int_k^{+\infty} S_Z(k') dk', \quad \Pi_T(k) = \int_k^{+\infty} S_T(k') dk', \quad (14)$$

where $S_Z(k)$ and $S_T(k)$ are the enstrophy and entropy transfer functions. They are obtained by angular integration of $\widehat{w^*(\mathbf{k})} \cdot (\mathbf{v} \cdot \nabla) \widehat{w(\mathbf{k})}$ and $\widehat{T^*(\mathbf{k})} \cdot (\mathbf{v} \cdot \nabla) \widehat{T(\mathbf{k})}$.

In our study, we replace the usual Fourier decompositions by spherical harmonics decompositions, and the angular integration of the Fourier coefficients by a summation of the spherical coefficients f_k^m over the degree $m = -k$ to $m = k$. The results are strictly equivalent to classical energy, enstrophy, and entropy fluxes and can be considered as such.

2. Energy and Enstrophy spectra

In Refs. [36,37], the authors show that a Kolmogorov like spectrum ($k^{-5/3}$) should be observed in three-dimensional Rayleigh-Bénard turbulence, while a Bolgiano-like spectrum ($k^{-11/5}$) is expected

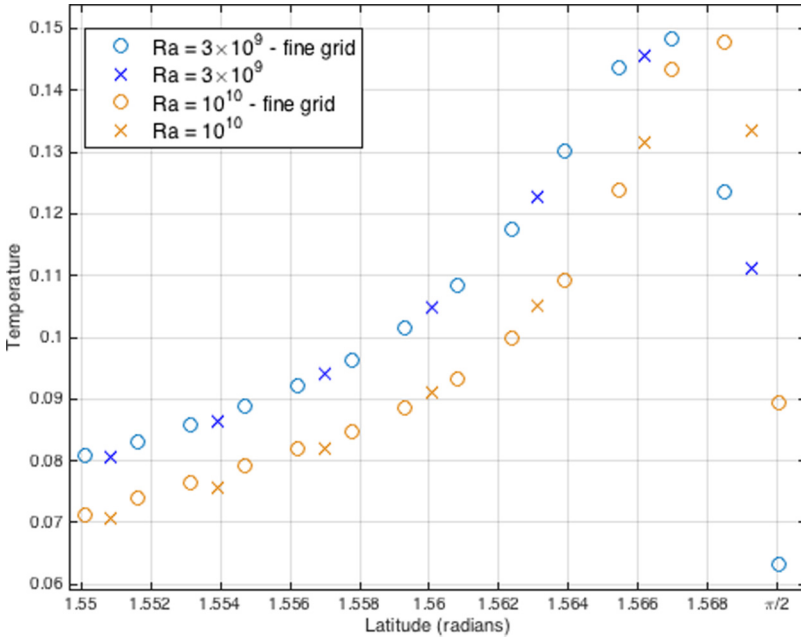


FIG. 15. Zoom on RMS of the temperature fluctuations as a function of the polar angle for $Ra = 3 \times 10^9$ and $Ra = 10^{10}$ at $Pr = 7$.

in two-dimensional turbulence due to the presence of the inverse cascade of kinetic energy. Energy and enstrophy spectra for various Rayleigh number simulations (from $Ra = 10^6$ to $Ra = 10^{10}$) are given in Figs. 16 and 17. We can observe that as the Rayleigh number increases, the energy (respectively,

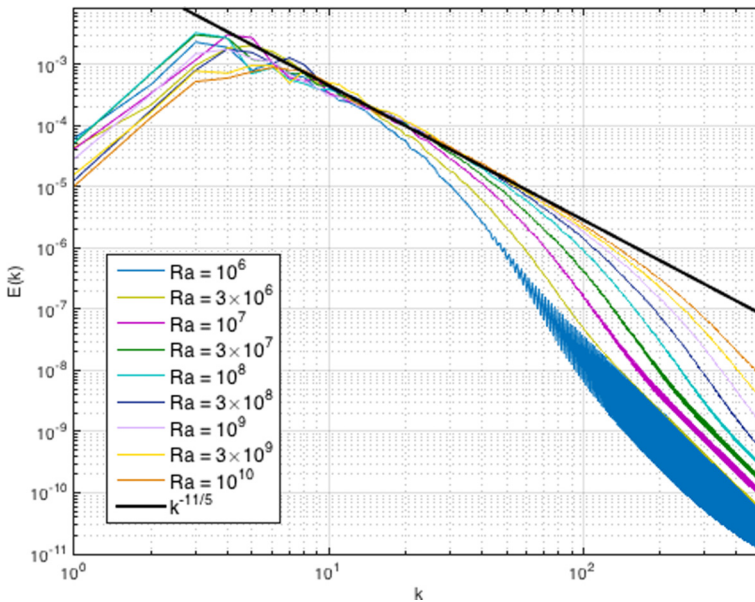


FIG. 16. Energy spectra for various Rayleigh number simulations (from $Ra = 10^6$ to $Ra = 10^{10}$) at $Pr = 7$. A Bolgiano regime can be clearly observed for high Rayleigh number values.

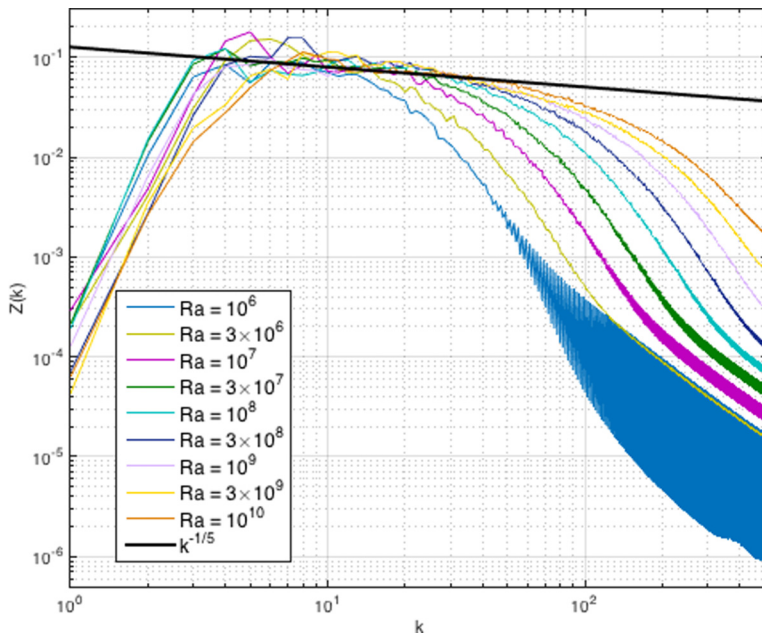


FIG. 17. Enstrophy spectra for various Rayleigh number simulations (from $Ra = 10^6$ to $Ra = 10^{10}$) at $Pr = 7$. A Bolgiano regime can be clearly observed for high Rayleigh number values.

enstrophy) spectra tend to follow a $k^{-11/5}$ (respectively, $k^{-1/5}$) scaling corresponding to the Bolgiano regime [36–39]. Our results are consistent with Verma *et al.* [36] and Kumar *et al.* [37] confirming the two-dimensional nature of our experiment with a strong kinetic energy inverse cascade which will be discussed below when we consider energy fluxes in Fig. 23. For low Rayleigh numbers this regime is observed only at large scales, which is consistent with the classical theory that predicts a Bolgiano-type regime from the largest scales to the Bolgiano scale and a Kolmogorov-type regime from the Bolgiano scale to the dissipation scale. The Bolgiano scale is supposed to decrease with the Rayleigh number, it is thus expected that the range of length scales for the Bolgiano regime increases with the Rayleigh number. We report in Fig. 18 the evolution in time of the energy spectrum for $Ra = 10^{10}$ and $Pr = 7$ from the beginning of the simulation up to the stationary state. As expected, we observe an increase of the energy at large scales as the structures are spread all over the bubble. The stationary state spectrum is smoother than the other spectra because it has been obtained by averaging 40 snapshots (and only two snapshots for the other spectra). High amplitude oscillations at small scales can be observed for $Ra = 10^6$ but not for other Rayleigh numbers. We do not have so far any explanation for these small-scale oscillations.

3. Entropy spectra

Entropy spectra for various Rayleigh number simulations (from $Ra = 10^6$ to $Ra = 10^{10}$) are given in Fig. 19. The entropy spectra present very strong oscillations. This oscillating behavior has been observed for Rayleigh-Bénard 2D turbulence by Vincent and Yuen in Ref. [40]. They obtained a scaling of $k^{-5/3}$ in their temperature spectrum. Mishra *et al.* [36,41–43] also observed this kind of oscillations (called *dual branches* in their articles) and they also proposed a theoretical explanation for this behavior. They predicted different scalings for the upper (k^{-2}) and the lower ($k^{-5/3}$ or $k^{-7/5}$ for a Kolmogorov or a Bolgiano regime) branches of the spectrum. However, the results they show in their papers do not fit well this prediction. We give in the Appendix additional details to explain the oscillations in our entropy spectra. These oscillations are actually related to the steep temperature gradient near the equator and therefore to the in-homogeneity of the mean temperature over the full

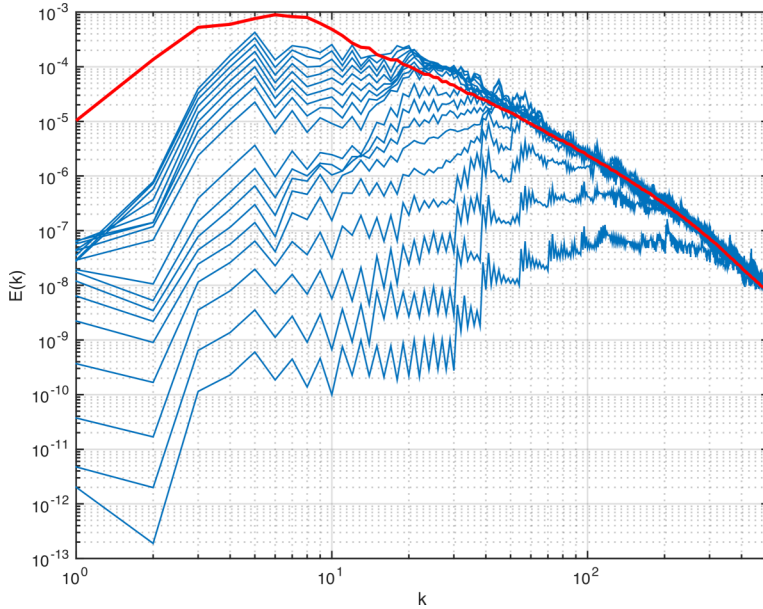


FIG. 18. Evolution of the energy spectrum with time from 0.2 to 3.6 (with a 0.2 nondimensional time step) at $Ra = 10^{10}$ and $Pr = 7$. Red spectrum: stationary state spectrum.

hemisphere. Nevertheless, these spectra over the full hemisphere are instructive. We can observe in our simulations that the spectra for high Rayleigh numbers tend to oscillate less and can be fit to a $k^{-3/5}$ scaling.

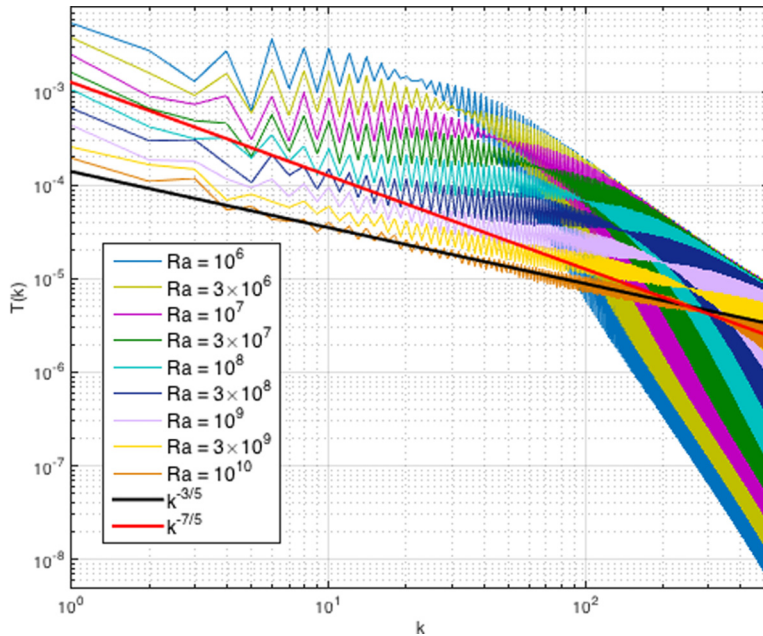


FIG. 19. Entropy spectra for various Rayleigh number simulations (from $Ra = 10^6$ to $Ra = 10^{10}$) at $Pr = 7$. A dual branch due to the averaged temperature profile can be observed.

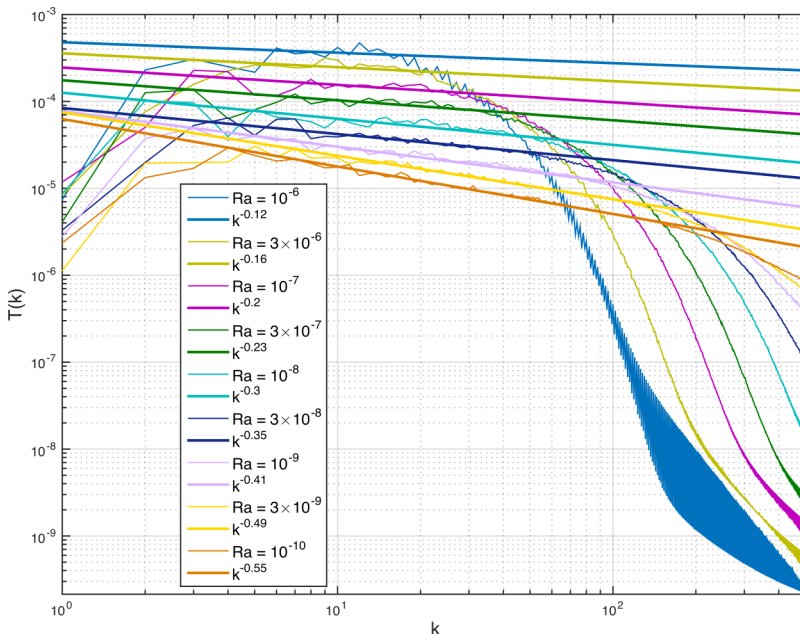


FIG. 20. Temperature fluctuations spectra for various Rayleigh number simulations (from $Ra = 10^6$ to $Ra = 10^{10}$).

This scaling does not correspond to a Bolgiano regime ($k^{-7/5}$) nor to a Kolmogorov regime ($k^{-5/3}$). To study these scalings we can remove the averaged temperature profile responsible for the oscillation. Doing so we can obtain the entropy spectra of the temperature fluctuations. The results are summarized in Fig. 20. We can observe that the scalings depend on the Rayleigh number and this dependency can be verified in the doubly logarithmic plot of the scaling coefficient versus the Rayleigh number in Fig. 21. We observe a scaling law with a slope of $\approx 1/6$. We have no explanation for this behavior. Since this has not been observed in any Rayleigh-Bénard convection experiment, it might be specific to our particular setup. However, we can still try to find a Bolgiano regime somewhere on the bubble. It is well known that the Bolgiano regime is very sensitive to the geometry and sometimes can be observed only in particular areas of the fluid [15]. It has been generally observed that the Bolgiano scale is of the same order as the length scale L of the cell, making it difficult to observe in the spectra the Bolgiano regime in the bulk. However, the area close to the equator is dominant and might hide a Bolgiano regime that would be present elsewhere in the bubble. It is also this region that gives rise to the observed scaling as explained in the Appendix. To verify this hypothesis, we decided to compute the fluctuations temperature spectra for three different Rayleigh number simulations ($Ra = 3 \times 10^6$, 10^8 , and 10^{10}) in the bulk: more specifically in the area corresponding to a polar angle going from 0 to $\pi/6$. As can be observed in Fig. 22, a $k^{-7/5}$ scaling is present at large scales on a range of one decade up to $k \simeq 150$ for high Rayleigh number simulations, but on a shorter range for low Rayleigh number simulations. This result confirms the presence of the Bolgiano regime already detected in the energy and enstrophy spectra. In the experiments on soap bubbles [9,10], Bolgiano scaling was observed locally outside the equatorial zone as well, so our results agree with these experiments. In short and to obtain this scaling for the temperature, the equatorial zone needs to be removed from the analysis. Our results are thus in good agreement with results of convective two-dimensional systems without boundary layers as in Rayleigh-Taylor or mean-gradient forced Rayleigh-Bénard turbulence. However, we refer to Ref. [13] for a detailed discussion about the statistical equivalence between Rayleigh-Taylor turbulence and Rayleigh-Bénard turbulence.

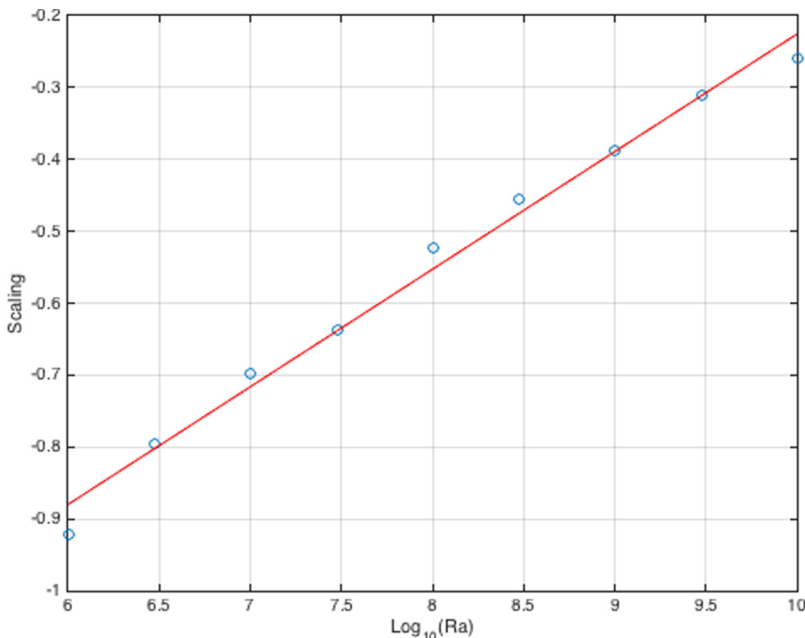


FIG. 21. Absolute value of the scaling exponent of the temperature fluctuations spectra as a function of the Rayleigh number. Slope of the linear fit $\approx 1/6$.

4. The link between the Bolgiano scale and the fluxes

For large scales, in the so-called Bolgiano regime, the temperature is supposed to act as an active scalar field whereas for small scales (below the Bolgiano scale) it is supposed to behave like a passive scalar field. So, energy, enstrophy, and entropy fluxes should reflect this transition from one regime to the other. This is exactly what we observe in our results. We believe that in our simulations we do not have a single Bolgiano scale but rather a range of scales where this transition occurs. Indeed, we observe in the three fluxes the existence of negative fluxes from a given scale (that depends on the Rayleigh number) to the largest scale, and positive fluxes from this particular scale to the dissipation scale. This phenomenon can be observed in Figs. 23, 24, and 25. If we plot the scales S_z of these zero crossing points versus the Rayleigh number, we obtain the graph in Fig. 26. We observe that the scales of the zero crossing points seem to follow a scaling law with exponent between -0.21 and -0.26 . The scales of these zero crossing points are located in the range of the Bolgiano scale. So we can speculate on the scaling of a global Bolgiano scale as a function of the Rayleigh number for our particular simulations: $L_B \propto Ra^{-1/4}$. The Bolgiano scale is very sensitive to the geometry of the setup and we cannot reliably compare our conjecture to any result found in the literature. For all simulations, in the range where the Bolgiano regime is observed, the fluxes do not present any plateau. This observation implies that we do not observe a constant flux cascade in this range.

V. DISCUSSION AND CONCLUDING REMARKS

We have presented numerical simulations of an original experiment for creating thermal convection. The purpose of the present paper was to detail the numerical simulations and analyze the global physical properties (Nusselt number, Reynolds number, spectra, fluxes) versus a characteristic of the fluid, the Rayleigh number. As mentioned above, to reach a stationary state for the simulations two additional dissipation terms were added to the temperature and to the velocity equations. For the stationary state achieved as described in the paper, we observed the following scaling for the Nusselt number: $Nu \propto Ra^{0.31}$ for $Pr = 7$. Concerning the Reynolds number, we observed two regimes

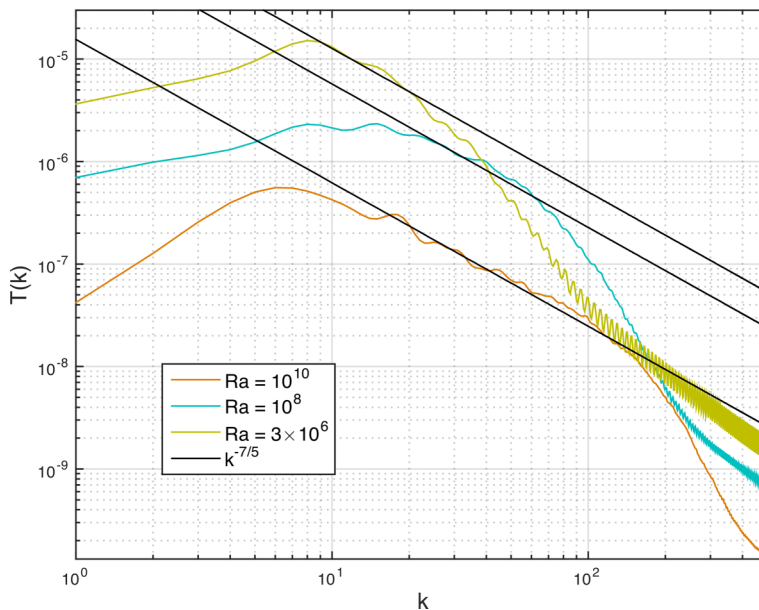


FIG. 22. Temperature fluctuations spectra computed in the pole area from 0 to $\pi/6$ rad at $\text{Pr} = 7$. The $k^{-7/5}$ scaling for high Rayleigh numbers confirms the presence of the Bolgiano regime.

versus the Rayleigh number, $\text{Re} \propto \text{Ra}^{0.43}$ and $\text{Re} \propto \text{Ra}^{0.55}$ (around $\text{Ra}^{1/2}$ if we consider a linear regression over the whole range of Rayleigh number) with a transition around Ra^8 . Even if this particular setup does not correspond to a Rayleigh-Bénard experiment, the values we obtain are

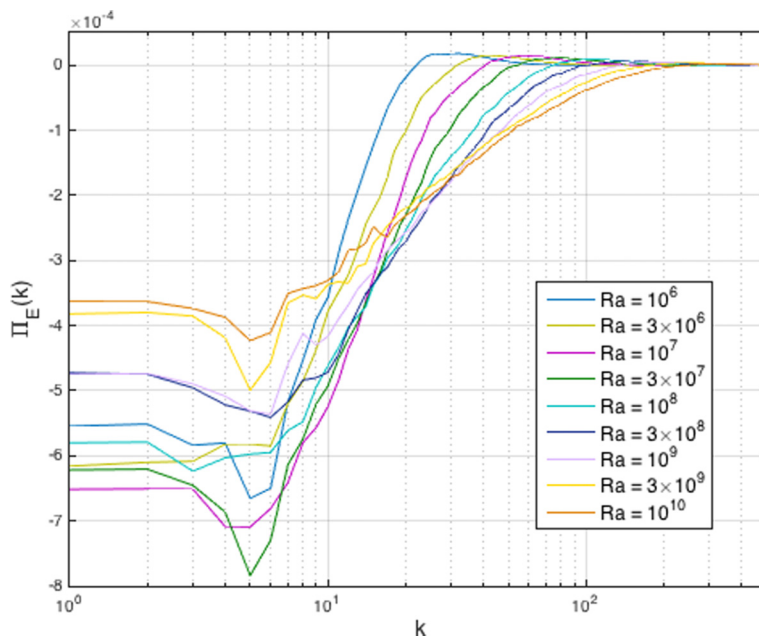


FIG. 23. Energy fluxes for various Rayleigh number simulations (from $\text{Ra} = 10^6$ to $\text{Ra} = 10^{10}$) at $\text{Pr} = 7$. The zero-crossing of the energy flux can be used as an indicator of the behavior of the Bolgiano scale with respect to the Rayleigh number.

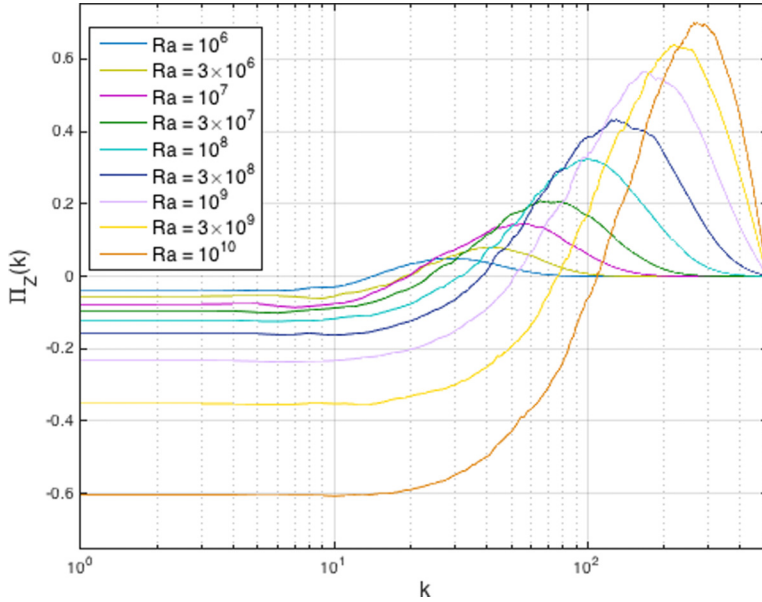


FIG. 24. Enstrophy fluxes for various Rayleigh number simulations (from $Ra = 10^6$ to $Ra = 10^{10}$) at $Pr = 7$. The zero-crossing of the enstrophy flux can be used as an indicator of the behavior of the Bolgiano scale with respect to the Rayleigh number.

quite close to the exponents found in the literature [26–31]. In particular, our scalings are quite close to the ones corresponding to the regime I_1 described by Grossmann and Lohse in their unifying theory [19–23]. This regime is described as the one where thermal and kinetic boundary layers

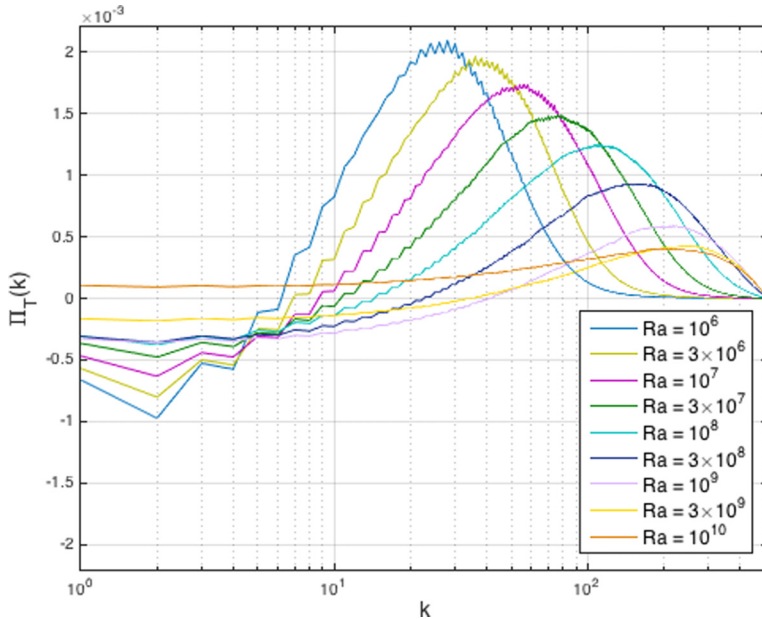


FIG. 25. Entropy fluxes for various Rayleigh number simulations (from $Ra = 10^6$ to $Ra = 10^{10}$) at $Pr = 7$. The zero-crossing of the entropy flux can be used as an indicator of the behavior of the Bolgiano scale with respect to the Rayleigh number.

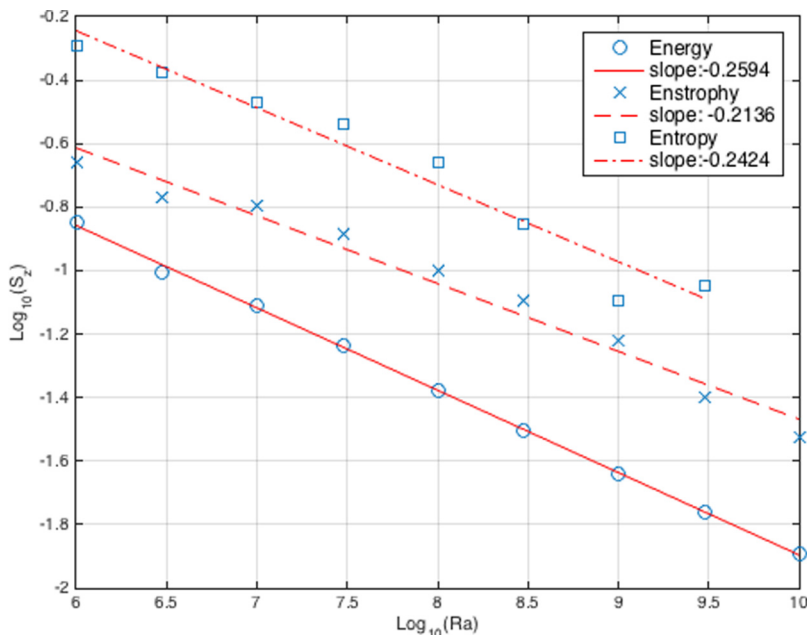


FIG. 26. Scales S_z of the zero crossing points for the energy, enstrophy, and entropy fluxes for various Rayleigh number simulations (from $Ra = 10^6$ to $Ra = 10^{10}$) at $Pr = 7$. These parameters can be used as proxies for the Bolgiano scale. A clear scaling in function of the Rayleigh number can be observed.

dominate the dissipation. Since we do not generate any large scale circulation in the bulk of the bubble, it is reasonable to expect a boundary layer dominated dissipation in our case.

Studying the spectra and the fluxes allowed us to assess other physical properties such as the Bolgiano regime and its corresponding scale. Scalings of $k^{-11/5}$ and $k^{-1/5}$ in the energy and enstrophy spectra have been detected: in a short range at large scales for low Rayleigh numbers, and in a larger range for high Rayleigh numbers. This observation indicates that the Bolgiano scale decreases as the Rayleigh number increases. Concerning the entropy spectra, we highlighted two important features:

(1) the gradient of temperature from almost 0 (at the pole) to 1 (at the equator) induces large (for low Rayleigh number simulations) or small (for high Rayleigh number simulations) oscillations in the spectra.

(2) the thermal boundary layer dominates the fluid over a large equatorial area.

Removing the averaged temperature profile allowed us to get rid of the oscillations but does not reduce the influence of the thermal boundary layer: we obtained the same scalings as with the complete temperature fields. However, removing the temperature field around the equator allowed us to uncover a Bolgiano scaling ($k^{-7/5}$) around the pole in the temperature fluctuations spectra. Indeed, removing the equatorial zone allows to remove the strong temperature gradient, which affects the spectra, as well as the effect of the coherent structures (thermal plumes as seen in Fig. 1) which render the fluctuations anisotropic. Another way to confirm the existence of a Bolgiano regime in our experiment is through the analysis of the fluxes. The fluxes show the existence of inverse transfers to large scales. The crossover from direct transfers at small scales to inverse transfers at larger scales occurs at a length scale which decreases with the Rayleigh number. If we identify this scale as the Bolgiano scale, its variation with the Rayleigh number turns out to be $L_B \propto Ra^{-1/4}$.

Despite the effects of geometry and unconventional heat injection, the system studied here turns out to obey scaling laws which resemble those from conventional cells. Further, the turbulence statistics turn out to obey Bolgiano like scaling for both energy and enstrophy and also for the temperature fluctuations in a localized region far from the equatorial boundary layer.

ACKNOWLEDGMENTS

The authors thank Gilles Carbou and Pierre Mounoud for fruitful discussions about the geometry and the metrics. The research is supported by the French Agence Nationale de la Recherche, under Grant *Cyclobulle* funding. The numerical simulations were run on PLAFRIM platform supported by University of Bordeaux and INRIA Bordeaux Sud-Ouest.

APPENDIX A: DIFFERENT SYSTEMS OF COORDINATES

We consider in this paper three kinds of coordinate systems: $\mathbf{C}_0(x_0, y_0, z_0)$, the usual 3D orthogonal Cartesian coordinates; $\mathbf{C}_1(r, \theta, \varphi)$, the usual 3D spherical coordinates; and $\mathbf{C}(x, y)$, a 2D orthogonal Cartesian coordinate system obtained by a stereographic projection onto the equatorial plane. The stereographic projection is a particular mapping that allows us to project a sphere onto a plane. The usual projection is defined on the entire sphere, but we use in this study a version restricted to the northern hemisphere. This mapping is bijective and preserves the angles: a Cartesian grid on the plane corresponds to a Cartesian grid on the surface of the sphere. However, this particular mapping is neither isometric nor area-preserving: the distances and the areas are not preserved. This feature forces us to detail the calculations of the different derivatives involved in the equations. Figure 27 illustrates the stereographic projection where a point P on the sphere is projected on P' on the equatorial plane.

The three kind of coordinates mentioned above are related to each other by the following equalities:

$$\begin{aligned} x_0 &= r \sin \theta \cos \varphi = \frac{2xr^2}{r^2 + x^2 + y^2} \\ y_0 &= r \sin \theta \sin \varphi = \frac{2yr^2}{r^2 + x^2 + y^2} \\ z_0 &= r \cos \theta = r \frac{r^2 - (x^2 + y^2)}{r^2 + x^2 + y^2} \end{aligned} \quad (\text{A1})$$

and

$$\begin{aligned} x &= \frac{r \sin \theta \cos \varphi}{1 + \cos \theta} = \frac{rx_0}{r + \sqrt{r^2 - (x_0^2 + y_0^2)}}, \\ y &= \frac{r \sin \theta \sin \varphi}{1 + \cos \theta} = \frac{ry_0}{r + \sqrt{r^2 - (x_0^2 + y_0^2)}}. \end{aligned} \quad (\text{A2})$$

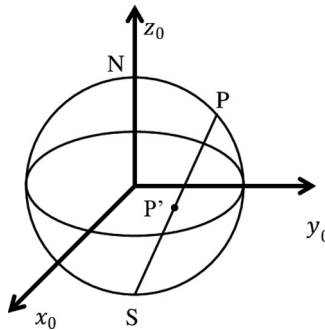


FIG. 27. Stereographic projection: the point P of coordinates (x_0, y_0, z_0) on the sphere is projected on P' of coordinates (x, y) on the plane. N and S denote, respectively, the north and south poles.

So any arc ds can be described using three-dimensional Cartesian or spherical coordinates:

$$\begin{aligned}
 ds^2 &= dx_0^2 + dy_0^2 + dz_0^2 \\
 &= \left(\frac{\partial x_0}{\partial r} dr + \frac{\partial x_0}{\partial \theta} d\theta + \frac{\partial x_0}{\partial \varphi} d\varphi \right)^2 + \left(\frac{\partial y_0}{\partial r} dr + \frac{\partial y_0}{\partial \theta} d\theta + \frac{\partial y_0}{\partial \varphi} d\varphi \right)^2 \\
 &\quad + \left(\frac{\partial z_0}{\partial r} dr + \frac{\partial z_0}{\partial \theta} d\theta + \frac{\partial z_0}{\partial \varphi} d\varphi \right)^2 \\
 &= h_r^2 dr^2 + h_\theta^2 d\theta^2 + h_\varphi^2 d\varphi^2,
 \end{aligned} \tag{A3}$$

with

$$\begin{aligned}
 h_r^2 &= \left(\frac{\partial x_0}{\partial r} \right)^2 + \left(\frac{\partial y_0}{\partial r} \right)^2 + \left(\frac{\partial z_0}{\partial r} \right)^2 = 1, \quad h_\theta^2 = \left(\frac{\partial x_0}{\partial \theta} \right)^2 + \left(\frac{\partial y_0}{\partial \theta} \right)^2 + \left(\frac{\partial z_0}{\partial \theta} \right)^2 = r^2, \\
 h_\varphi^2 &= \left(\frac{\partial x_0}{\partial \varphi} \right)^2 + \left(\frac{\partial y_0}{\partial \varphi} \right)^2 + \left(\frac{\partial z_0}{\partial \varphi} \right)^2 = r^2 \sin^2 \theta.
 \end{aligned} \tag{A4}$$

It can also be described using the stereographic coordinates obtained by projection onto the equatorial plane:

$$ds^2 = dx_0^2 + dy_0^2 + dz_0^2 = h_r^2 dr^2 + h_\theta^2 d\theta^2 + h_\varphi^2 d\varphi^2 = h_x^2 dx^2 + h_y^2 dy^2. \tag{A5}$$

Coefficients h_x and h_y are usually called the Lamé coefficients and can be used to calculate the components of a given basis family into any other basis. The calculation of the Lamé coefficients (h_x, h_y) and the metrics corresponding to the stereographic coordinates are detailed in the next section.

APPENDIX B: THE LAMÉ COEFFICIENTS

The Lamé coefficients can be used to calculate the various operators involved in the Navier-Stokes equations. If one denotes by $(\mathbf{e}_i)_{i=1,2,3}$ an orthonormal basis of \mathbb{R}^3 then the gradient of any scalar field ϕ can then be written as

$$\nabla \phi = \sum_{i=1}^3 \frac{1}{h_i} \frac{\partial \phi}{\partial q_i} \mathbf{e}_i, \tag{B1}$$

where q_i is the i th coordinate and h_i is the corresponding Lamé coefficient. In the same way, the divergence of any vector field \mathbf{B} can be written in a general form as

$$\nabla \cdot \mathbf{B} = \frac{1}{h_1 h_2 h_3} \left[\frac{\partial (B_1 h_2 h_3)}{\partial q_1} + \frac{\partial (B_2 h_1 h_3)}{\partial q_2} + \frac{\partial (B_3 h_1 h_2)}{\partial q_3} \right], \tag{B2}$$

where B_i denotes the i th component of \mathbf{B} in the basis $(\mathbf{e}_i)_i$.

The Laplacian of any scalar function ϕ is given by

$$\Delta \phi = \frac{1}{h_1 h_2 h_3} \left[\frac{\partial}{\partial q_1} \left(\frac{h_2 h_3}{h_1} \frac{\partial \phi}{\partial q_1} \right) + \frac{\partial}{\partial q_2} \left(\frac{h_1 h_3}{h_2} \frac{\partial \phi}{\partial q_2} \right) + \frac{\partial}{\partial q_3} \left(\frac{h_1 h_2}{h_3} \frac{\partial \phi}{\partial q_3} \right) \right]. \tag{B3}$$

The total time derivative is then given by

$$\frac{D\phi}{Dt} = \frac{\partial \phi}{\partial t} + \frac{u_1}{h_1} \frac{\partial \phi}{\partial q_1} + \frac{u_2}{h_2} \frac{\partial \phi}{\partial q_2} + \frac{u_3}{h_3} \frac{\partial \phi}{\partial q_3}. \tag{B4}$$

Any vector \mathbf{M} belonging to a sphere of radius r and center O , expressed in the three-dimensional framework $\mathbf{C}_0(x_0, y_0, z_0)$ as $\mathbf{M} = x_0 \mathbf{i}_0 + y_0 \mathbf{j}_0 + z_0 \mathbf{k}_0$, can be written using its (x, y) stereographic

coordinates:

$$\mathbf{M} = \frac{2r^2x}{r^2+x^2+y^2}\mathbf{i}_0 + \frac{2r^2y}{r^2+x^2+y^2}\mathbf{j}_0 + r\frac{r^2-x^2-y^2}{r^2+x^2+y^2}\mathbf{k}_0. \quad (\text{B5})$$

The Lamé coefficients corresponding to the stereographic coordinates are then given by the following formula:

$$\begin{aligned} h_x = |\mathbf{h}_x| &= \left| \frac{\partial \mathbf{M}}{\partial x} \right| \\ &= \left| \frac{2r^2}{(x^2+y^2+r^2)^2} [(r^2-x^2+y^2)\mathbf{i}_0 - 2yx\mathbf{j}_0 - 2xr\mathbf{k}_0] \right| \\ &= \frac{2r^2}{r^2+x^2+y^2} \\ h_y = |\mathbf{h}_y| &= \left| \frac{\partial \mathbf{M}}{\partial y} \right| \\ &= \left| \frac{2r^2}{(x^2+y^2+r^2)^2} [-2yx\mathbf{i}_0 + (r^2-y^2+x^2)\mathbf{j}_0 - 2yr\mathbf{k}_0] \right| \\ &= \frac{2r^2}{r^2+x^2+y^2}. \end{aligned} \quad (\text{B6})$$

As stated above, the three Lamé coefficients in the \mathbf{C}_0 Cartesian system of coordinates are $h_i = h_{x_0} = h_{y_0} = h_{z_0} = 1, \forall i \in \{1, 2, 3\}$. In the \mathbf{C}_1 spherical basis we have $h_1 = h_r = 1$, $h_2 = h_\theta = r$, $h_3 = h_\varphi = r \sin \theta$, and in the \mathbf{C} stereographic system of coordinates we have $h_1 = h_2 = \frac{2r^2}{x^2+y^2+r^2} (= h_x = h_y)$.

To write any three-dimensional vector (belonging to the sphere) with its stereographic coordinates, we need to write the Cartesian vectors ($\mathbf{i}_0, \mathbf{j}_0, \mathbf{k}_0$) in function of ($\mathbf{h}_x, \mathbf{h}_y$). We thus need to complete the stereographic basis ($\mathbf{h}_x, \mathbf{h}_y$) with a vector \mathbf{h}_r orthogonal to the tangent plane at (x_0, y_0, z_0) spanned by ($\mathbf{h}_x, \mathbf{h}_y$). We can choose for \mathbf{h}_r the radial position vector \mathbf{M} . We then obtain the following equations:

$$\begin{pmatrix} \mathbf{h}_x \\ \mathbf{h}_y \\ \mathbf{h}_r \end{pmatrix} = \begin{pmatrix} \frac{2r^2(r^2-x^2+y^2)}{(r^2+x^2+y^2)^2} & \frac{-4yxr^2}{(r^2+x^2+y^2)^2} & \frac{-4xr^3}{(r^2+x^2+y^2)^2} \\ \frac{-4yxr^2}{(r^2+x^2+y^2)^2} & \frac{2r^2(r^2-y^2+x^2)}{(r^2+x^2+y^2)^2} & \frac{-4yr^3}{(r^2+x^2+y^2)^2} \\ \frac{2r^2x}{r^2+x^2+y^2} & \frac{2yr^2}{r^2+x^2+y^2} & \frac{r(r^2-y^2-x^2)}{r^2+x^2+y^2} \end{pmatrix} \begin{pmatrix} \mathbf{i}_0 \\ \mathbf{j}_0 \\ \mathbf{k}_0 \end{pmatrix}. \quad (\text{B7})$$

This matrix has to be inverted to write the basis vectors ($\mathbf{i}_0, \mathbf{j}_0, \mathbf{k}_0$) in function of the basis vectors ($\mathbf{h}_x, \mathbf{h}_y, \mathbf{h}_r$):

$$\begin{pmatrix} \mathbf{i}_0 \\ \mathbf{j}_0 \\ \mathbf{k}_0 \end{pmatrix} = \begin{pmatrix} \frac{r^2+y^2-x^2}{2r^2} & \frac{-xy}{r^2} & \frac{2x}{r^2+x^2+y^2} \\ \frac{-xy}{r^2} & \frac{r^2+x^2-y^2}{2r^2} & \frac{2y}{r^2+x^2+y^2} \\ \frac{-x}{r} & \frac{-y}{r} & \frac{r^2-x^2-y^2}{r(r^2+x^2+y^2)} \end{pmatrix} \begin{pmatrix} \mathbf{h}_x \\ \mathbf{h}_y \\ \mathbf{h}_r \end{pmatrix}. \quad (\text{B8})$$

Adapting the previous formula to our ($\mathbf{h}_x, \mathbf{h}_y, \mathbf{h}_r$) basis, the various operators involved in the Navier-Stokes equations can be written using the stereographic projection. For instance, we obtain for the gradient operator of a scalar field ϕ :

$$\nabla \phi = \left(\frac{r^2+x^2+y^2}{2r^2} \right)^2 \left(\frac{\partial \phi}{\partial x} \mathbf{h}_x + \frac{\partial \phi}{\partial y} \mathbf{h}_y \right). \quad (\text{B9})$$

The corresponding Laplace operator is given by

$$\Delta\phi = \left(\frac{r^2 + x^2 + y^2}{2r^2}\right)^2 \left(\frac{\partial^2\phi}{\partial x^2} + \frac{\partial^2\phi}{\partial y^2}\right). \quad (\text{B10})$$

The divergence of a vector field \mathbf{U} in stereographic coordinates is given by the following formula:

$$\nabla \cdot \mathbf{U} = \frac{\partial u}{\partial x} + \frac{\partial v}{\partial y} - \frac{4r^2}{r^2 + x^2 + y^2}(xu + yv), \quad (\text{B11})$$

where (u, v) denotes the components of \mathbf{U} in the 2D stereographic basis $(\mathbf{h}_x, \mathbf{h}_y)$. In the same way, the projection of the Laplacian of a vector field $\mathbf{u} = u\mathbf{h}_x + v\mathbf{h}_y$ onto the stereographic coordinates plane is given by

$$\begin{aligned} \nabla^2 \mathbf{u} = & \left[\frac{(r^2 + x^2 + y^2)^2}{4r^4} \left(\frac{\partial^2 u}{\partial x^2} + \frac{\partial^2 u}{\partial y^2} \right) - u - (r^2 + x^2 + y^2) \left(x \frac{\partial u}{\partial x} + y \frac{\partial u}{\partial y} + y \frac{\partial v}{\partial x} - x \frac{\partial v}{\partial y} \right) \right] \mathbf{h}_x \\ & + \left[\frac{(r^2 + x^2 + y^2)^2}{4r^4} \left(\frac{\partial^2 v}{\partial x^2} + \frac{\partial^2 v}{\partial y^2} \right) - v - (r^2 + x^2 + y^2) \left(x \frac{\partial u}{\partial y} - y \frac{\partial u}{\partial x} + x \frac{\partial v}{\partial x} + y \frac{\partial v}{\partial y} \right) \right] \mathbf{h}_y. \end{aligned} \quad (\text{B12})$$

APPENDIX C: THE METRICS

Another way to derive the equations in the equatorial plane is to use directly the metrics between a tangent plane to the hemisphere and the equator plane. The stereographic transform from the south pole i_S yields from Eq. (A2) with $r = 1$:

$$x = \frac{x_0}{1 + z_0} \quad y = \frac{y_0}{1 + z_0} \quad (\text{C1})$$

and its inverse i_S^{-1}

$$x_0 = \frac{2x}{1 + x^2 + y^2} \quad y_0 = \frac{2y}{1 + x^2 + y^2} \quad z_0 = \frac{1 - x^2 - y^2}{1 + x^2 + y^2}. \quad (\text{C2})$$

Thus, the Jacobian matrix is given by

$$J_{i_S^{-1}} = \begin{bmatrix} \partial_x x_0 & \partial_y x_0 \\ \partial_x y_0 & \partial_y y_0 \\ \partial_x z_0 & \partial_y z_0 \end{bmatrix}. \quad (\text{C3})$$

Then the metrics is $g = g_{ij} = J_{i_S^{-1}}^t J_{i_S^{-1}}$ and its inverse $g^{-1} = g^{ij}$. So it yields with Einstein indexing for a scalar f and a vector $U = (u, v)$:

$$\begin{aligned} (\nabla f)^i &= \partial^i f = g^{ij} \partial_j f, \quad (U \cdot V)^i = (U \cdot gV)_i, \quad \text{div} U = \frac{1}{\sqrt{|g|}} \partial_i (\sqrt{|g|} U^i), \\ \Delta f &= \text{div}(\nabla f) = \frac{1}{\sqrt{|g|}} \partial_i (\sqrt{|g|} g^{ij} \partial_j f), \quad \Delta U = g^{ij} (\nabla_{\partial_i} \nabla_{\partial_j} U - \nabla_{\nabla_{\partial_i} \partial_j} U), \end{aligned} \quad (\text{C4})$$

where the covariant derivative is a vector defined by $\nabla_{\partial_i} \partial_j = \Gamma_{ij}^k \partial_k$ with Christoffel symbols $\Gamma_{ij}^k = \frac{1}{2} c_g (\partial_i c_g \delta^{jk} + \partial_j c_g \delta^{ik} - \partial_k c_g \delta^{ij})$ for $g = c_g id$ where δ is the Kronecker symbol and id the identity.

From these definitions it comes

$$J_{i_S^{-1}} = \begin{bmatrix} \frac{2(1-x^2+y^2)}{(1+x^2+y^2)^2} & \frac{-4xy}{(1+x^2+y^2)^2} \\ \frac{-4xy}{(1+x^2+y^2)^2} & \frac{2(1+x^2-y^2)}{(1+x^2+y^2)^2} \\ \frac{-4x}{(1+x^2+y^2)^2} & \frac{-4y}{(1+x^2+y^2)^2} \end{bmatrix}, \quad (C5)$$

which gives the conformal metrics

$$g = \frac{4}{(1+x^2+y^2)^2} \begin{bmatrix} 1 & 0 \\ 0 & 1 \end{bmatrix} \quad (C6)$$

and its inverse

$$g^{-1} = \frac{(1+x^2+y^2)^2}{4} \begin{bmatrix} 1 & 0 \\ 0 & 1 \end{bmatrix}. \quad (C7)$$

Then it follows

$$\begin{aligned} (\nabla f)^i &= \frac{(1+x^2+y^2)^2}{4} (\nabla f)_i \\ (U \cdot \nabla)^i f &= (U \cdot g g^{-1} \nabla)_i f = (U \cdot \nabla)_i f \\ (\operatorname{div} U)^i &= (\operatorname{div} U)_i - \frac{4xu + 4yv}{1+x^2+y^2} \\ (\Delta f)^i &= \frac{(1+x^2+y^2)^2}{4} (\Delta f)_i. \end{aligned} \quad (C8)$$

It remains to compute two difficult terms $(U \cdot \nabla)^i U$ and $(\Delta U)^i$.

Using the Christoffel symbols,

$$\begin{aligned} \Gamma_{11}^1 &= \frac{-2x}{1+x^2+y^2}, & \Gamma_{11}^2 &= \frac{2y}{1+x^2+y^2}, & \Gamma_{12}^1 &= \frac{-2y}{1+x^2+y^2}, & \Gamma_{12}^2 &= \frac{-2x}{1+x^2+y^2} \\ \Gamma_{21}^1 &= \frac{-2y}{1+x^2+y^2}, & \Gamma_{21}^2 &= \frac{-2x}{1+x^2+y^2}, & \Gamma_{22}^1 &= \frac{2x}{1+x^2+y^2}, & \Gamma_{22}^2 &= \frac{-2y}{1+x^2+y^2}, \end{aligned} \quad (C9)$$

we can compute

$$\begin{aligned} (U \cdot \nabla)^i U &= \nabla_U U = u \nabla_{\partial_x} U + v \nabla_{\partial_y} U \\ &= u^2 \nabla_{\partial_x} \partial_x + u(\partial_x u) \partial_x + uv \nabla_{\partial_x} \partial_y + u(\partial_x v) \partial_y \\ &\quad + uv \nabla_{\partial_y} \partial_x + v(\partial_y u) \partial_x + v^2 \nabla_{\partial_y} \partial_y + v(\partial_y v) \partial_y \\ &= (U \cdot \nabla)_i U + \frac{2}{1+x^2+y^2} \begin{bmatrix} -xu^2 - 2yuv + xv^2 \\ yu^2 - 2xuv - yv^2 \end{bmatrix} \end{aligned} \quad (C10)$$

and

$$(\Delta U)^i = g^{11} (\nabla_{\partial_x} \nabla_{\partial_x} U - \nabla_{\nabla_{\partial_x} \partial_x} U) + g^{22} (\nabla_{\partial_y} \nabla_{\partial_y} U - \nabla_{\nabla_{\partial_y} \partial_y} U), \quad (C11)$$

where, for instance,

$$\nabla_{\partial_x} U = \begin{bmatrix} \partial_x u + u \Gamma_{11}^1 + v \Gamma_{12}^1 \\ \partial_x v + u \Gamma_{21}^2 + v \Gamma_{12}^2 \end{bmatrix} \quad (C12)$$

and

$$\nabla_{\partial_x} \nabla_{\partial_x} U = \begin{bmatrix} \partial_x^2 u + \partial_x(u\Gamma_{11}^1 + v\Gamma_{12}^1) + (\partial_x u + u\Gamma_{11}^1 + v\Gamma_{12}^1)\Gamma_{11}^1 + (\partial_x v + u\Gamma_{11}^2 + v\Gamma_{12}^2)\Gamma_{12}^1 \\ \partial_x^2 v + \partial_x(u\Gamma_{11}^2 + v\Gamma_{12}^2) + (\partial_x u + u\Gamma_{11}^1 + v\Gamma_{12}^1)\Gamma_{11}^2 + (\partial_x v + u\Gamma_{11}^2 + v\Gamma_{12}^2)\Gamma_{12}^2 \end{bmatrix}. \quad (\text{C13})$$

So it comes finally

$$(\Delta U)^i = \frac{(1+x^2+y^2)^2}{4} (\Delta U)_i - U - (1+x^2+y^2) \begin{bmatrix} x\partial_x u + y\partial_y u + y\partial_x v - x\partial_y v \\ x\partial_y u - y\partial_x u + x\partial_x v + y\partial_y v \end{bmatrix}. \quad (\text{C14})$$

APPENDIX D: ENTROPY SPECTRUM

Since the spherical harmonics are defined on the whole sphere, we had to numerically extend our bubble on the southern hemisphere. This had been made by a zero-padding extension on the southern hemisphere. However, to determine if the dual branches are due to this extension, we have performed the computations for other extensions:

- (1) 1-padding extension,
- (2) symmetrical extension.

The temperature on the bubble is decreasing from $T = 1$ at the equator to almost 0 at the pole (the temperature is equal to 0 in the beginning of the simulation but reaches a small value, depending on the Rayleigh number, when the stationary state is established). So we can observe a steep temperature profile in the boundary layer going from a small value to 1 at the equator (see Fig. 12). To study this steep variation, we have also performed computations on a hemisphere by keeping only the averaged temperature field. In addition to these calculations, we have calculated numerically and mathematically the spectrum of a spherical Heaviside function (zero on the northern hemisphere and one on the southern hemisphere). Since the mean temperature profile has a steep gradient near the equator, the Heaviside function is a good tool to examine the role of the mean temperature profile on the spectrum. This calculation is thus carried out to illustrate how a steep variation of the mean temperature near the equator affects the spectrum in the absence of temperature fluctuations since only the mean temperature is retained. As it turns out, it is this steep variation that engenders the oscillations in the spectrum.

First, let us recall the definition of the spherical harmonic coefficients on the whole sphere:

$$\begin{aligned} f_k^m &= \int_0^{2\pi} \int_0^\pi f(\theta, \varphi) \overline{Y_k^m(\theta, \varphi)} \sin(\theta) d\theta d\varphi \\ &= \sqrt{\frac{2k+1}{4\pi} \frac{(k-m)!}{(k+m)!}} \int_0^{2\pi} \int_0^\pi f(\theta, \varphi) P_k^m[\cos(\theta)] e^{-im\varphi} \sin(\theta) d\theta d\varphi. \end{aligned} \quad (\text{D1})$$

It can be noticed that if the function f does not depend on φ then $f_k^m = 0$ if $m \neq 0$. So, for the spherical Heaviside function we only have to calculate

$$f_k^0 = \sqrt{\frac{2k+1}{4\pi}} 2\pi \int_0^{\pi/2} P_k^0[\cos(\theta)] \sin(\theta) d\theta. \quad (\text{D2})$$

We then obtain for the energy spectrum

$$E(k) = \frac{\pi(2k+1)}{2} \left\{ \int_0^{\pi/2} P_k^0[\cos(\theta)] \sin(\theta) d\theta \right\}^2. \quad (\text{D3})$$

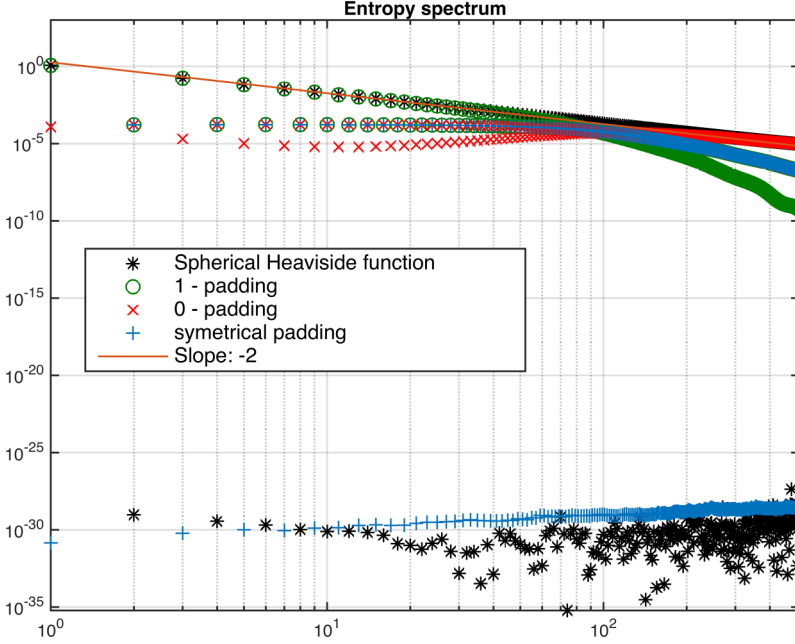


FIG. 28. Entropy spectra for various functions and extensions. At the top the odd modes of a Heaviside function (black stars) are superimposed to the straight line of slope -2 , the odd modes of the 1-padding spectrum are also superimposed on this line up to $k \simeq 70$ and then decrease (green circles). In the middle, the even modes of the 1-padding spectrum (green circles), of the 0-padding spectrum (red crosses), and of the symmetrical padding spectrum (blue pluses) are superimposed. Below, the odd modes of the 0-padding extension are shown (in red). In the bottom of the figure, the even modes of Heaviside function and the odd modes of the symmetrical padding spectrum are very small and near zero. The spectra are shown for the mean temperature field for $Ra = 3 \times 10^9$ with different padding schemes.

Using the expansion of the Legendre polynomials we can explicitly calculate the energy:

$$E(k) = \frac{\pi(2k+1)}{2} \left\{ \int_0^{\pi/2} \frac{1}{2^k} \sum_{j=0}^{[k/2]} (-1)^j \binom{k}{j} \binom{2(k-j)}{k} [\cos(\theta)]^{k-2j} \sin(\theta) \right\}^2, \quad (D4)$$

where $[k/2]$ denotes the largest integer smaller than (or equal to) $k/2$, and $\binom{k}{j}$ is the Newton binomial coefficient. The integration on θ can be easily calculated, and we obtain

$$E(k) = \frac{\pi(2k+1)}{2} \left\{ \frac{1}{2^k} \sum_{j=0}^{[k/2]} (-1)^j \frac{[2(k-j)]!}{(k-j)!j!(k-2j+1)!} \right\}^2. \quad (D5)$$

We can check that $E(k) = 0$ if k is strictly positive and even. We give here the first few values for $k = 0 \dots 7$:

$$E(0) = \frac{\pi}{2}; \quad E(1) = \frac{3\pi}{8}; \quad E(3) = \frac{7\pi}{128}; \quad E(5) = \frac{11\pi}{512}; \quad E(7) = \frac{375\pi}{32768}.$$

Our numerical computations give the same results as the exact values. These coefficients are given with black stars in Fig. 28. It can be noticed that the nonzero coefficients of the Heaviside function (the odd modes) show a decay with exponent close (but not equal) to -2 . This is very close to the spectrum of the Heaviside function obtained with the Fourier coefficients when working with cartesian coordinates. For this former case, the theoretical values for the energy spectrum are

$E(k) = \frac{1}{4\pi^2 k^2}$, obtained from the corresponding Fourier coefficients. Verma *et al.* mentioned this same value in Refs. [36,41]. This slope can be observed in particular in Fig. 10 of Ref. [36]. They obtained this value for the even wave-numbers with a rigorous calculation of the Fourier coefficients. They also note that their lower branch shows neither Kolmogorov ($k^{-3/5}$) nor Bolgiano ($k^{-7/5}$) spectrum, whereas, in our numerical experiments, we can obtain the Bolgiano scaling in the pole area (far from the boundary layers), as explained in the main part of this article.

In our results, the k^{-2} slope corresponds also to the upper branch (odd modes) of the 1-padding extension for large scales (Fig. 28). We can conclude that this upper branch for the large scales is due to the 1-padding extension on the southern hemisphere and behaves as a Heavy side functions. Further, we can observe that the upper branch (even modes) of the 0-padding extension and the lower branch (even modes) of the 1-padding extension are exactly the same. They are also exactly the same as the upper branch (even modes) of the symmetrical-padding extension. This branch where the three different paddings are superimposed is therefore due to the presence of the steep but not infinite gradient near the equator on the upper hemisphere side.

So, our conclusion from this short study is that our numerical entropy spectra show oscillations because the mean temperature profile has a steep variation near the equator on the upper hemisphere. These oscillations can be removed by removing the averaged temperature profile from the temperature fields as presented in the text. They are present for different padding schemes, but their amplitudes depend on the padding scheme used. The obtained numerical values of the spectral amplitudes are thus correct and the oscillations are not numerical artifacts of the simulation but correspond to the effect of a steep variation of temperature between almost 0 up to 1. The amplitudes of these oscillations have been obtained with a rigorous mathematical calculation for the spherical Heaviside function. Further, the amplitude of these oscillations is small only for the 0-padding scheme used for calculating the spectra shown in the main text. The scaling in $-3/5$ observed for high Ra is the result of this gradient, as shown in Fig. 28.

-
- [1] R. Kraichnan and D. Montgomery, Two-dimensional turbulence, *Rep. Prog. Phys.* **43**, 547 (1980).
 - [2] R. Kraichnan, Turbulent thermal convection at arbitrary Prandtl numbers, *Phys. Fluids* **5**, 1374 (1962).
 - [3] R. Kraichnan, Inertial ranges in two-dimensional turbulence, *Phys. Fluids* **10**, 1417 (1967).
 - [4] J.-D. Debus, M. Mendoza, S. Succi, and H. J. Herrmann, Poiseuille flow in curved spaces, *Phys. Rev. E* **93**, 043316 (2016).
 - [5] M. Mendoza, S. Succi, and H. J. Herrmann, Flow through randomly curved manifolds, *Sci. Rep.* **3**, 3106 (2013).
 - [6] J. Cho and L. Polvani, The emergence of jets and vortices in freely evolving, shallow-water turbulence on a sphere, *Phys. Fluids* **8**, 1531 (1995).
 - [7] H. Benard, Les tourbillons cellulaires dans une nappe de liquide—Méthodes optiques d’observation et d’enregistrement, *J. Phys. Theor. Appl.* **10**, 254 (1901).
 - [8] O. M. Rayleigh, On convection currents in a horizontal layer of fluid, when the higher temperature is on the under side, *Philos. Mag. Ser. 6* **32**, 529 (1916).
 - [9] F. Seychelles, Y. Amarouchene, M. Bessafi, and H. Kellay, Thermal Convection and Emergence of Isolated Vortices in Soap Bubbles, *Phys. Rev. Lett.* **100**, 144501 (2008).
 - [10] F. Seychelles, F. Ingremeau, C. Pradere, and H. Kellay, From Intermittent to Nonintermittent Behavior in Two-Dimensional Thermal Convection in a Soap Bubble, *Phys. Rev. Lett.* **105**, 264502 (2010).
 - [11] T. Meuel, Y.-L. Xiong, P. Fischer, C.-H. Bruneau, M. Bessafi, and H. Kellay, Intensity of vortices: From soap bubbles to hurricanes, *Sci. Rep.* **3**, 3455 (2013).
 - [12] Y.-L. Xiong, P. Fischer, and C.-H. Bruneau, Numerical simulations of two-dimensional turbulent thermal convection on the surface of a soap bubble, in *Proceedings of the 7th International Conference on Computational Fluid Dynamics (ICCFD7-3703)* (2012).

- [13] G. Boffetta and A. Mazzino, Incompressible Rayleigh-Taylor turbulence, *Annu. Rev. Fluid Mech.* **49**, 119 (2017).
- [14] G. Boffetta, F. De Lillo, and A. Musacchio, Bolgiano scale in confined Rayleigh-Taylor turbulence, *J. Fluid Mech.* **690**, 426 (2012).
- [15] D. Lohse and K.-Q. Xia, Small-scale properties of turbulent Rayleigh-Bénard convection, *Annu. Rev. Fluid Mech.* **42**, 335 (2010).
- [16] J. Boussinesq, *Théorie analytique de la chaleur mise en harmonie avec la thermodynamique et avec la théorie mécanique de la lumière* (Gauthier-Villars, Paris, 1903).
- [17] P. Angot, C.-H. Bruneau, and P. Fabrie, A penalization method to take into account obstacles in incompressible viscous flow, *Numer. Math.* **81**, 497 (1999).
- [18] C. H. Bruneau and M. Saad, The 2D lid-driven cavity problem revisited, *Comput. Fluids* **35**, 326 (2006).
- [19] S. Grossmann and D. Lohse, Characteristic scales in Rayleigh-Bénard convection, *Phys. Lett. A* **173**, 58 (1993).
- [20] S. Grossmann and D. Lohse, Scaling in thermal convection: A unifying view, *J. Fluid Mech.* **407**, 27 (2000).
- [21] S. Grossmann and D. Lohse, Thermal Convection for Large Prandtl Number, *Phys. Rev. Lett.* **86**, 3316 (2001).
- [22] S. Grossmann and D. Lohse, Prandtl and Rayleigh number dependence of the Reynolds number in turbulent thermal convection, *Phys. Rev. E* **66**, 016305 (2002).
- [23] S. Grossmann and D. Lohse, On geometry effects in Rayleigh-Bénard convection, *J. Fluid Mech.* **486**, 105 (2003).
- [24] S. Grossmann and D. Lohse, Fluctuations in turbulent Rayleigh-Bénard convection: The role of plumes, *Phys. Fluids* **16**, 4462 (2004).
- [25] E. Sanvicente, S. Giroux-Julien, C. Menezo, and H. Bouia, Transitional natural convection flow and heat transfer in an open channel, *Inter. J. Thermal Sci.* **63**, 87 (2013).
- [26] J. Niemela, L. Skrbek, K. R. Sreenivasan, and R. Donnelly, Turbulent convection at very high Rayleigh numbers, *Nature* **404**, 837 (2000).
- [27] J. Niemela and K. R. Sreenivasan, Confined turbulent convection, *J. Fluid Mech.* **481**, 355 (2003).
- [28] J. Niemela and K. R. Sreenivasan, Turbulent convection at high Rayleigh numbers and aspect ratio 4, *J. Fluid Mech.* **557**, 411 (2006).
- [29] G. Ahlers, D. Funfschilling, and E. Bodenschatz, Transitions in heat transport by turbulent convection at Rayleigh numbers up to 10^{15} , *New J. Phys.* **11**, 123001 (2009).
- [30] A. Nikolaenko and G. Ahlers, Nusselt Number Measurements for Turbulent Rayleigh-Bénard Convection, *Phys. Rev. Lett.* **91**, 084501 (2003).
- [31] D. Funfschilling, E. Brown, A. Nikolaenko, and G. Ahlers, Heat transport by turbulent Rayleigh-Bénard convection in cylindrical cells with aspect ratio one and larger, *J. Fluid Mech.* **536**, 145 (2005).
- [32] S. Kenjereš and K. Hanjalić, Numerical insight into flow structure in ultraturbulent thermal convection, *Phys. Rev. E* **66**, 036307 (2002).
- [33] A. Maystrenko, C. Resagk, and A. Thess, Structure of the thermal boundary layer for turbulent Rayleigh-Bénard convection of air in a long rectangular enclosure, *Phys. Rev. E* **75**, 066303 (2007).
- [34] R. DuPuits, C. Resagk, A. Tilgner, F. Busse, and A. Thess, Structure of thermal boundary layers in turbulent Rayleigh-Bénard convection, *J. Fluid Mech.* **572**, 231 (2007).
- [35] A. Belmonte, A. Tilgner, and A. Libchaber, Temperature and velocity layers in turbulent convection, *Phys. Rev. E* **50**, 269 (1994).
- [36] M. Verma, A. Kumar, and A. Pandey, Phenomenology of buoyancy-driven turbulence: Recent results, *New J. Phys.* **19**, 025012 (2017).
- [37] A. Kumar, A. G. Chatterjee, and M. K. Verma, Energy spectrum of buoyancy-driven turbulence, *Phys. Rev. E* **90**, 023016 (2014).
- [38] R. Bolgiano, Turbulent spectra in a stably stratified atmosphere, *J. Geophys. Res.* **64**, 2226 (1959).
- [39] R. Bolgiano, Structure of turbulence in stratified media, *J. Geophys. Res.* **67**, 3015 (1962).
- [40] A. P. Vincent and D. A. Yuen, Plumes and waves in two-dimensional turbulent thermal convection, *Phys. Rev. E* **60**, 2957 (1999).

- [41] P. Mishra and M. Verma, Energy spectra and fluxes for Rayleigh-Bénard convection, [Phys. Rev. E **81**, 056316 \(2010\)](#).
- [42] M. K. Verma, P. Mishra, M. Chandra, and S. Paul, Energy spectra in Rayleigh-Benard convection, [J. Phys.: Conf. Ser. **318**, 082014 \(2011\)](#).
- [43] A. Pandey, M. K. Verma, and P. K. Mishra, Scaling of heat flux and energy spectrum for very large Prandtl number convection, [Phys. Rev. E **89**, 023006 \(2014\)](#).